Heliyon 10 (2024) e29408

Contents lists available at ScienceDirect

Heliyon

journal homepage: www.cell.com/heliyon

Research article

Combined experimental and first principles look into (Ce, Mo) doped $BiVO_4$

Tasnim Ahmed Mahi [a], Quazi Shafayat Hossain [a], Sadiq Shahriyar Nishat [b], Shahran Ahmed [a,d], M.N.I. Khan [c], Muhammad Shahriar Bashar [d], Shirin Akter Jahan [e], Umme Sarmeen Akhtar [e], Sharmin Jahan [f], Fariha Chowdhury [g], Khandker Saadat Hossain [h], Ahmad Irfan [i], Imtiaz Ahmed [a,*]

[a] *Materials Science Research Laboratory, Department of Electrical and Electronic Engineering, University of Dhaka, Dhaka-1000, Bangladesh*
[b] *Department of Materials Science and Engineering, Rensselaer Polytechnic Institute, Troy, NY, USA*
[c] *Materials Science Division, Atomic Energy Centre, Dhaka-1000, Bangladesh*
[d] *Institute of Energy Research and Development, Bangladesh Council of Scientific and Industrial Research, Dhaka-1205, Bangladesh*
[e] *Institute of Glass and Ceramic Research and Testing, Bangladesh Council of Scientific and Industrial Research, Dhaka-1205, Bangladesh*
[f] *Institute of Food Science and Technology, Bangladesh Council of Scientific and Industrial Research, Dhaka-1205, Bangladesh*
[g] *Biomedical and Toxicological Research Institute, Bangladesh Council of Scientific and Industrial Research, Dhaka-1205, Bangladesh*
[h] *Nanophysics and Soft Matter Laboratory, Department of Physics, University of Dhaka, Dhaka-1000, Bangladesh*
[i] *Department of Chemistry, College of Science, King Khalid University, PO. Box 9004, Abha 61413, Saudi Arabia*

A B S T R A C T

Here we investigated the effects of Ce and Mo doping on hydrothermally synthesized bismuth vanadate $BiVO_4$ nanoparticles (NPs). The existence of monoclinic scheelite and tetragonal zircon phases of NPs was validated from Rietveld refinement of the powdered X-ray diffraction, room temperature Raman, and Fourier-transform infrared spectroscopy. The co-doping of Bi and V sites with respective Ce and Mo dopants in a mixed tetragonal zircon and monoclinic scheelite phases of $BiVO_4$ lattice was corroborated from high-resolution transmission electron microscopy and X-ray photoelectron spectroscopy. The photoluminescence measurements revealed enhancement of photo-generated carrier recombination in (Ce, Mo) co-doped $BiVO_4$ NPs which may have hampered its photocatalytic efficiency in degrading the methylene blue dye. The simulations based on Hubbard U corrected density functional theory (DFT+U) suggest that Mo and Ce co-doping introduced deep impurity states which may have facilitated the photo-generated carrier recombination detrimental to photocatalytic performance. The UV-vis diffuse reflectance measurements provided evidence for the presence of these defect states. In summary, this work may have presented a comprehensive experimental analysis of (Ce, Mo) doped $BiVO_4$ supported by DFT simulations.

1. Introduction

The ternary oxide bismuth vanadate $BiVO_4$ has sparked widespread research interests as a promising photocatalytic material due to its (i) proper electronic band gap, (ii) steep optical absorption edge in the visible range of the electromagnetic spectrum, (iii) photo-stability, and (iv) abundance and benign nature [1–4]. Out of its tetragonal scheelite (*ts*), monoclinic scheelite (*ms*), and tetragonal zircon (*tz*) structures; the *ms* phase turned out to be the most photosensitive phase [5]. The *ab initio* density functional theory (DFT) based simulations have been the guiding star for comprehending the functional properties of $BiVO_4$ relevant to photocatalytic performance [6–18]. Numerous methods like noble metal loading, heterojunction, co-catalysts deposition, semiconductor

* Corresponding author.
E-mail address: imtiaz@du.ac.bd (I. Ahmed).

https://doi.org/10.1016/j.heliyon.2024.e29408
Received 27 November 2023; Received in revised form 28 March 2024; Accepted 8 April 2024

Available online 15 April 2024

recombination, facet control, morphology control, microstructure control, and metal doping were put forward to modulate the photocatalytic activity of $BiVO_4$ [2,19–27]. Among these techniques, doping turned out to be a simple, low-cost, and efficient way of tuning the photocatalytic activity of $BiVO_4$.

The rare earth (RE) lanthanide elements containing *f* orbitals (Ce, Eu, La, Gd, Nd, Yb, and Sm) and transition metals (TMs) (Y, Zr, Fe, Co, Ni) having *d* orbitals preferentially go to Bi-site in $BiVO_4$ to reduce the photo-generated carrier recombination. For example, the Ce^{3+} ion (102 pm) with $4f^1$ electron tends to replace Bi^{3+} (103 pm) ion due to comparable ionic radii and played important role in determining the photocatalytic performance [28–30]. The unperturbed V^{5+} site leaves the [VO_4] tetrahedral chain in $BiVO_4$ lattice almost undisturbed that favors *ms* phase over the *tz* phase. The Ce^{3+} dopants in *ms* $BiVO_4$ phase can localize holes and prevent them from recombining with electrons [31]. Due to similar ionic radii, the Mo^{6+} (59 pm) dopant can act as an n-type hexavalent dopant for the V^{5+} (54 pm) [32]. The DFT simulations also confirmed the Mo^{6+} as V-site dopants in $BiVO_4$ lattice [33,34]. The Mo^{6+} having one excess electron compared to the host V^{5+} forms shallow n-type donor impurity states that can be activated at room temperature to boost up photo-generated carrier separation [35–40].

The co-doping of $BiVO_4$ with multiple dopants has proven to be an efficient way of enhancing photocatalytic performances [41]. The co-doping of the Bi-site can be facilitated by a combination of RE/TM elements such as (La, Gd), (Er, Y), (Gd, Y), (Yb, Er), and (Yb, Tm, Er) [42–46]. In the case of V-site, the co-doping attempts have been made through (W, Mo), and (W, Ti) combinations to enhance the photocatalytic activity of $BiVO_4$ [47,48]. Moreover, co-doping of combined Bi and V sites with the chemical formula $Bi_{1-x}A_xV_{1-y}B_yO_4$ where A = Fe, Zr, Yb, Ti, and B = W, Mo have shown promising photocatalytic results [41,49–51]. Since RE element Ce and TM Mo are prominent Bi and V-site dopants in the case of mono-doped $BiVO_4$, their combined effect in $Bi_{1-x}Ce_xV_{1-y}Mo_yO_4$ co-doped structure deserves much attention and rigorous investigation. The 10% Ce doping of the Bi site in mono-doped $Bi_{0.90}Ce_{0.1}VO_4$ was shown to provide the best photocatalytic performance [31]. For Mo mono-doping in the V site of BVO, the notable photocatalytic performance was achieved at 2-3% doping concentrations [32,52]. Moreover, in the V-cite, the Mo doping concentration beyond 3% tends to distort the [VO_4] tetrahedral chains triggering the phase transition from the monoclinic to the tetragonal structure [30]. In addition, Mo concentration higher than 3% led to the formation of detrimental defect states hampering n-type conductivity [8,53]. Hence the Ce and Mo doping concentrations can be fixed at 10% and 2%, respectively.

Here we synthesized undoped, Ce and Mo mono-doped and (Ce, Mo) co-doped bismuth vanadate NPs following the hydrothermal method with chemical formulas $BiVO_4$, $Bi_{0.90}Ce_{0.10}VO_4$, $BiV_{0.98}Mo_{0.02}O_4$ and $Bi_{0.90}Ce_{0.10}V_{0.98}Mo_{0.02}O_4$, respectively. The phase evolution among *ms* and *tz* was studied from X-ray diffraction, Raman, and Fourier-transform infrared spectroscopy. The high-resolution transmission electron microscopy and X-ray photoelectron spectroscopy confirmed the Ce and Mo co-doping of respective Bi and V sites in mixed *ms-tz* $BiVO_4$ lattice. The field emission scanning electron microscopy confirmed the NP size to be ~ 20 nm. The steady-state photoluminescence revealed significant photo-generated carrier recombination in (Ce, Mo) co-doped $Bi_{0.90}Ce_{0.10}V_{0.98}Mo_{0.02}O_4$ NPs. The (Ce, Mo) co-doping also deteriorated the photocatalytic performance of $Bi_{0.90}Ce_{0.10}V_{0.98}Mo_{0.02}O_4$ in degrading the methylene blue (MB) dye. To the best of our knowledge, it is hard to find detailed DFT simulations of the electronic structure of (Ce, Mo) co-doped $Bi_{1-x}Ce_xV_{1-y}Mo_yO_4$ structure. We performed reliable DFT+U simulations and showed that the Ce and Mo dopants introduced deep impurity states that can act as photo-generated recombination centers and may have hampered the photocatalytic performance which is at par with our experimental findings. Moreover, increased defect density was confirmed by diffuse reflectance measurements. The irregular agglomeration and grain growth were also observed in FESEM measurements. Overall, this work may have provided an in-depth experimental analysis of functional properties of (Ce, Mo) co-doped $BiVO_4$ supported with DFT simulation.

2. Methodology

2.1. Computational details

The Vienna *Ab Initio* Simulation Package (VASP) was used to carry out spin-polarized simulations facilitated by the projector augmented wave (PAW) method within the framework of ab initio DFT [54,55]. The PAW treats Bi-$5d^{10}6s^26p^3$, V-$3p^63d^44s^1$, O-$2s^22p^4$, Ce-$5s^25p^64f^15d^16s^2$, and Mo-$4p^64d^55s^1$ as valence electrons. The $2\times2\times1$ supercell containing 96 atoms was considered for all simulations. Two Bi atoms were replaced by Ce atoms to form 12.5% Ce doped $BiVO_4$ supercell. The Mo-doped supercell had one V atom replaced by a Mo atom to emulate 6.25% doping. The (Ce, Mo) co-doped supercell was created with 12.5% Ce and 6.25% Mo doping concentrations. The k-space integrations in the Brillouin zone were facilitated by $2\times2\times2$ Monkhorst Pack grid k-points mesh to perform structural relaxation until Hellmann–Feynman forces and the self-consistent total energy reached 0.01 eV/Å and 10^{-5} eV, respectively. The plane-wave energy cut-off was set to 500 eV. The computational complexities and accuracy of the DFT simulation depend on the type of functional used to model the unknown electron exchange-correlation [56,57]. The localized V-3*d* dilutes the Coulomb interaction in GGA-PBE functional that requires boosting by the parameter U and following our previous work, we used $U = 4.8$ eV in Bi-*6p*, $U = 3.1$ eV in V-*3d* and $U = 2$ eV in O-*2p* [13,58–62]. In the case of the Ce and Mo atoms, the optimum values of the U were set to 3 and 2.3 eV on Ce-$4f$ and Mo-*4d*, respectively [31,34,63,64].

2.2. Sample preparation

The AR grade $Bi(NO_3)_3.5H_2O$ and NH_4VO_3 were dissolved with proper stoichiometry in HNO_3 and deionized (DI) water, respectively in case of undoped $BiVO_4$. The solutions were mixed under continuous magnetic stirring for 1 h. In cases of 10% Ce doped $Bi_{0.90}Ce_{0.10}VO_4$, 2% Mo doped $BiV_{0.98}M_{0.02}O_4$ and (Ce = 10%, Mo = 2%) co-doped $Bi_{0.90}Ce_{0.10}V_{0.98}M_{0.02}O_4$ samples, AR grade $Ce(NO_3)_3.6H_2O$ and $(NH_4)_2MoO_4$ precursors were used in stoichiometric proportion. The solution pH was kept to ~ 10 by adding

the required amount of NH_4OH in all cases. For each sample, the mixture was heated to 180 °C for 24 h in an oven by loading it in a 100 ml Teflon-lined stainless steel autoclave. The solution was agitated by subsequent vortex mixing and sonication. The precipitate resulting from centrifugation (8,000 rpm; 10 min; 4 cycles) and washing in DI water and ethanol, was dried at 120 °C for 24 h. The dried sample was collected and hand-milled for 1 h. The powdered sample was sintered subsequently at 400 °C for 2 h. The sintered undoped, Ce, Mo, and (Ce, Mo) co-doped samples were termed BVO, CBVO, MBVO, and CMBVO, respectively. For doped cases, the unsintered as-prepared samples were labeled as CBVO-A, MBVO-A, and CMBVO-A.

Photocatalytic Sample Preparation: The proper amount of MB dye was dissolved into DI water to obtain 100 ml of 10 ppm MB solutions. The BVO, CBVO, MBVO, and CMBVO NPs were dispersed as photocatalytic material to prepare 1 g/L solution. The pH was set to 10 by adding NH_4OH in the mixture of MB dye and the photocatalyst. The solution became a suspension as the adsorption-desorption equilibrium persisted after being subjected to vigorous magnetic stirring for 30 min in the dark. The mixture was kept under magnetic stirring while irradiated by simulated solar radiation facilitated by a Hg-Xe lamp. The stirring prevented the MB concentration gradient from occurring in the solution and thereby eliminated spurious degradation effects. The photocatalyst material was removed from the dye solution by several high-speed centrifuging cycles (10, 000 rpm, 7 cycles). The absorption spectra of the dye solution were recorded to estimate the degradation effect once every 30 min.

2.3. Characterization techniques

The sample sintering was facilitated by Muffle Furnaces (Nabertherm LT 5/14 & Kejia M1700). The powdered X-ray Diffraction (XRD) patterns within an angular range of 10° to 80° were obtained using a Rigaku SmartLab SE multipurpose XRD system with Cu Kα radiation ($\lambda = 0.15418$ nm) at 35 kV accelerating potential with an emission current of 20 mA. The AVO 18 Research Scanning Electron Microscope with Energy Dispersive X-ray Spectroscopy (EDX, EDAX Team) and a Field Emission Scanning Electron Microscopy (FESEM, JEOL 7610F) coupled with EDX Model: JED 2300 were used to perform NPs morphology, chemical purity analysis, and spatial elemental scans. The Transmission Electron Microscopy (TEM) images were obtained at 200 kV by Talos F200X. The Thermo Fischer Scientific X-ray Photoelectron Spectrometer was used to carry out Kα monochromated photoelectron spectroscopy of the NPs. The photoelectron binding energy calibration was done with 284.8 eV C-*1s* level as reference. The Horiba Scientific Confocal Raman Microscope LabRAM HR Evolution with 532 nm laser excitation was used to obtain the Raman spectra of the NPs. The absorption bands due to chemical bond vibrations were detected by the PerkinElmer Spectrum Fourier Transform Infrared (FTIR) spectrometer. The steady-state photoluminescence (PL) spectra of the NPs are recorded with 260 nm excitation in a Shimadzu RF-6000 Spectro Fluorophotometer. The UV-vis diffuse reflectance spectroscopy (DRS) was done with Shimadzu UV-2600i UV–vis–NIR spectrometer. The photocatalytic efficiency of the NPs was evaluated from UV-Vis absorption spectra recorded by the Shimadzu UV-1900i spectrometer.

3. Results and discussion

3.1. X-ray diffraction analysis

The XRD patterns of BVO, CBVO-A, CBVO, MBVO-A, MBVO, CMBVO-A, and CMBVO NPs with Miller indices are shown in Fig. 1(a). The detailed Rietveld refinements of all the XRD patterns are presented in Fig. S1 of Electronic Supplementary Information (ESI). The experimental crystallographic parameters are benchmarked against that of the GGA-PBE+U relaxed structures in Table S1. The *ms* phase (JCPDS 014-0688/ICSD-100602) having point group C_{2h}^6 and space group $C2/c$ (15) prevailed in BVO, CBVO, MBVO-A, and MBVO NPs. For as-product 10% Ce doped $Bi_{0.90}Ce_{0.10}VO_4$ (CBVO-A) NPs, the mixed *ms* and *tz* phases (JCPDS 14-0133/ICSD-100733, with point group C_{4h}^{19} and space group $I41/amd$ (141)) were observed. In the (Ce, Mo) co-doped $Bi_{0.90}Ce_{0.10}V_{0.98}M_{0.02}O_4$ NPs, both as-product (CMBVO-A, $\chi^2 = 4.2$) and sintered (CMBVO) samples displayed mixed *ms-tz* phases.

From the full-wave-half-maxima analysis of the (−221) XRD peak, the crystallite size D was estimated for all samples using the standard Debye-Scherrer's formula [65]. The values of defect density and strain were also estimated and displayed in Table S2 of ESI. It is evident that sintering at 400 °C enhances crystalline size, and reduces dislocation density and strain. In addition, sintering helped to attain *ms* purity in CBVO from a mixed *ms-tz* phase of CBVO-A as-prepared NPs. This may help to achieve better photocatalytic performances compared to the as-synthesized NPs [66,67]. Hence only sintered NPs were considered for the subsequent measurements.

Now we analyze the effect of doping and sintering temperature from the XRD peak shift in magnified view as displayed in Fig. 1(b)-(d). In all three 2θ ranges, the common thing to note is that XRD peaks are shifted towards lower diffraction angles for sintered samples (CBVO, MBVO, and CMBVO) compared to the as-prepared ones (CBVO-A, MBVO-A, and CMBVO-A). This shift can be attributed to a reduction in strain due to better crystallinity achieved from sintering [42]. The effect of doping can be comprehended by observing the peak shift of the sintered BVO, CBVO, MBVO, and CMBVO NPs. The negative 2θ shift is present in all mono and co-doped samples. This is expected as the Mo^{6+} have larger ionic size relative to host V^{5+}, respectively. This size mismatch increases the d-spacing which in turn sifted the peaks to lower diffraction angles [28,32,68].

The tetragonal scheelite phase was absent due to higher synthesis temperature (180 °C) and pH value (10) [69–72]. It is well established that the *tz* phase appears during the start of hydrothermal reaction independent of pH level [71,72]. But as the reaction progresses, the *tz* phase dissolves, and the *ms* phase starts to form for pH ≥ 7 [73,74]. Since the precursor solution pH was kept fixed at ~ 10, the *ms* phase prevailed in BVO. The 10% Ce doing may have inhibited the complete *tz* to *ms* transformation of the as-prepared CBVO-A and the mixed *ms-tz* phase existed. The sintering helped to achieve the full *tz* to *ms* transformation in CBVO. The

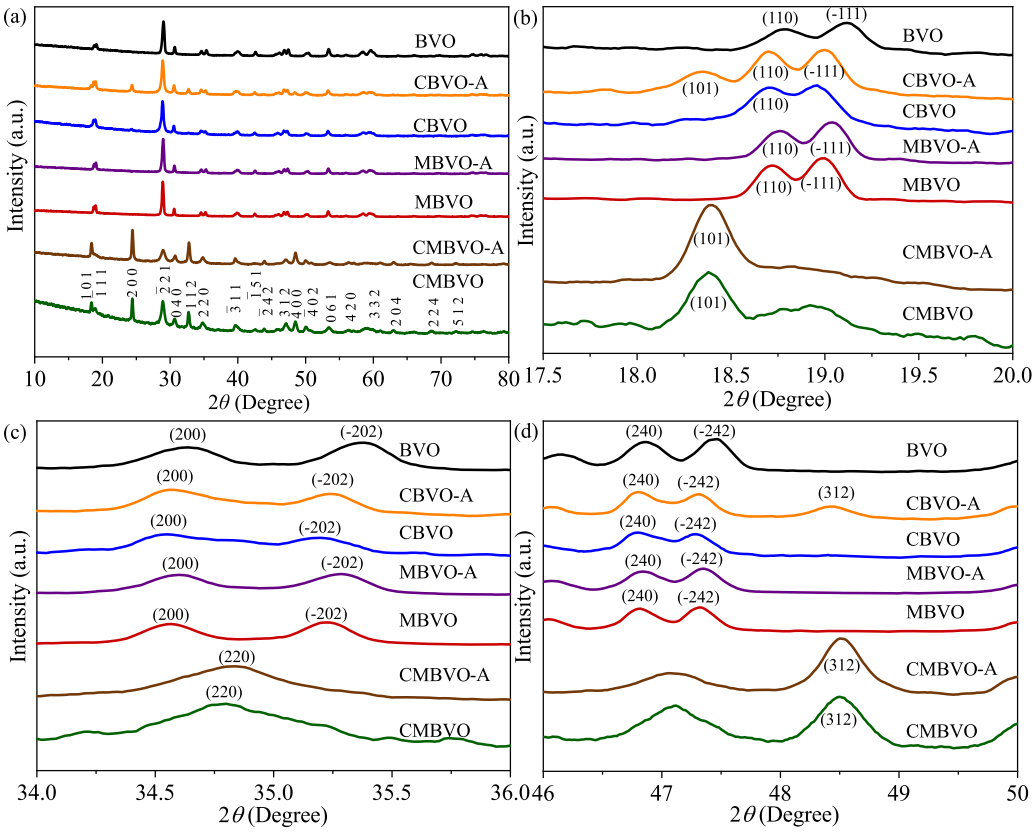

Fig. 1. (a) XRD patterns and magnified view to display peaks shifts in the 2θ range of (b) 17.5-20°, (c) 34-36° and (d) 46-50° of BVO, CBVO-A, CBVO, MBVO-A, MBVO, CMBVO-A, and CMBVO NPs.

relatively small (2%) Mo dopant did not hinder the complete *tz* to *ms* in MBVO-A sample. But for the (Gd = 10%, Mo = 2%) co-doped samples, the mixed *ms-tz* phase persisted regardless of the sintering. We speculate that the presence of Gd and Mo dopants prevented the *ms* phase purity from occurring in both CMBVO-A and CMBVO. For the two mixed-phase CBVO-A and CMBVO samples, the percentage of the monoclinic phase ζ_{ms} was estimated from the normalized intensities $I_{ms}^{(121)}$ and $I_{tz}^{(200)}$ corresponding to (121) and (200) diffraction peaks *ms* and *tz* phases, respectively as

$$\zeta_{ms} = \frac{I_{ms}^{(121)}}{I_{ms}^{(121)} + I_{tz}^{(200)}}, \tag{1}$$

and displayed in Table S1.

3.2. Raman analysis

The phonon vibrational spectra of *ms* $BiVO_4$ originate from $\Gamma = 8A_g + 10B_g + 8A_u + 10B_u$ consisting of 18 internal, 15 external, and 3 acoustic modes [13,75]. Among these symmetry-related 36 modes, only 13 modes defined by $\Gamma_{Raman} = 3A_g + 5B_g + 5E_g$ turned out to be Raman active [18]. The room temperature Raman spectra of BVO, CBVO, MBVO, and CMBVO were displayed in Fig. 2, and corresponding band assignments were shown in Table S3. Now for Ce substitutional doping of Bi site, due to very similar ionic sizes Ce^{3+} and Bi^{3+}, once expects very low crystal deformation of the *ms* phase of the BVO. The same is true for Mo-doped $BiV_{0.98}Mo_{0.02}O_4$ as Mo^{6+} and V^{5+} share similar ionic size and the ms phase purity persisted. Hence for both Ce and Mo mono-doped samples, we did not observe any significant variation in phonon energy, and this resulted in similar Raman peak positions as that of undoped *ms* BVO [30,31,40,52,76]. All samples have external lattice modes that stem Raman bands near 114 and 186 cm^{-1} which are not phase-specific [77]. The Raman bands that appeared at 335, 365, 710 and 811 cm^{-1} corroborate the *ms* phase purity in BVO, MBVO and CBVO samples [78,79]. The Raman peaks at 335 and 365 cm^{-1} are characteristic to asymmetric B_g and symmetric A_g deformation of $[VO_4]^{3-}$ tetrahedron, respectively. The asymmetric B_g and symmetric A_g stretching of V-O bonds correspond to 710 and 811 cm^{-1} Raman bands, respectively [2]. The presence of the *tz* phase in the CMBVO sample can be prescribed by Raman bands at 250 cm^{-1} owing to the stretching vibration of Bi-O bonds. Moreover, the Raman bands near 764 and 855 cm^{-1} in the CMBVO sample further confirm the presence of the *tz* phase in it [80,81]. The coexistence of characteristic Raman bands of *ms* (335, 365, 710 and 811 cm^{-1}) and *tz* (250, 764 and 855 cm^{-1}) phase validate the presence of *tz-ms* mixed phase in the co-doped CMBVO sample.

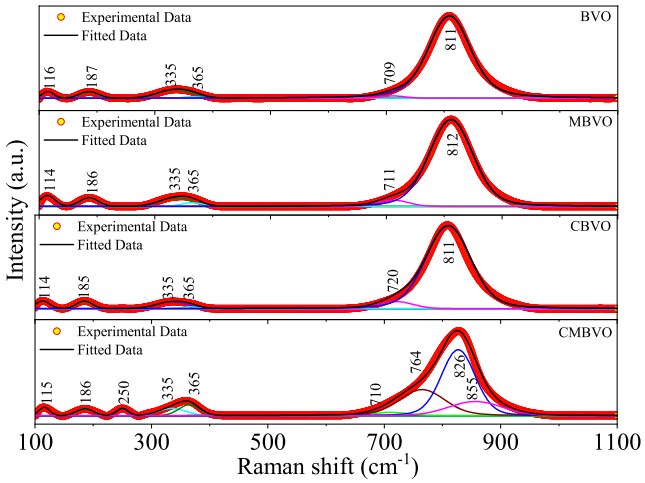

Fig. 2. Room temperature Raman spectra of BVO, MBVO, CBVO, and CMBVO NPs.

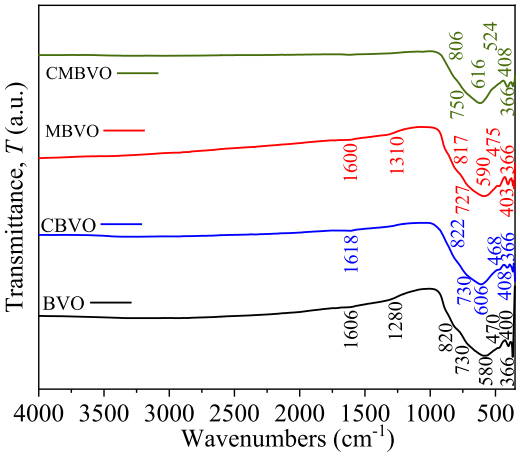

Fig. 3. FTIR spectra of BVO, CBVO, MBVO, and CMBVO NPs.

3.3. Fourier transform infrared spectroscopy

The FTIR spectra of BVO, CBVO, MBVO, and CMBVO are presented in Fig. 3, and the corresponding atomic bond vibrations are displayed in Table S4 [82]. The Bi-O bond stretching vibrations created weak IR absorption near 366 and 408 cm^{-1}. The absorption near 470 cm^{-1} may arise from the symmetric bending vibrations $[VO_4]^{3-}$. The anti-symmetric stretching of the V-O bond stems from the FTIR bands in the range 580-620 cm^{-1}. The VO_4^{3-} stretching modes have originated the weak absorption band near 730-750 cm^{-1} [83–86]. The symmetric stretching of the V-O bond emanated the absorption near 820 cm^{-1}. The Bi-O stretching vibrations remained unchanged in undoped, mono-doped, and co-doped samples. The antisymmetric stretching of the V-O bond of undoped BVO shifted to a higher wavenumber in cases of Ce, Mo mono-doped, and (Ce, Mo) co-doped samples [87,88]. Moreover, the symmetric stretching of the V-O bond was shifted towards the lower wavenumber in the (Ce, Mo) doped sample. In BVO and MBVO samples, the IR absorption band near 1300 cm^{-1} can be assigned to the stretching vibration of the C = O bond in adsorbed atmospheric CO_2 in the samples. The absorption near 1600 cm^{-1} in BVO, CBVO, and MBVO samples correspond to the bending vibration of H_2O molecules present in the samples. We assumed that both CO_2 and H_2O/OH^- ions adsorbed in the photocatalyst have ambient origin. This ambient adsorption is quite common for $BiVO_4$ [38,42,89]. The presence of the IR bands due to the stretching vibration of water molecules indicates the tendency of water adsorption at the surface which could be beneficial for their photocatalytic activity [90].

3.4. Surface morphology analysis

The FESEM micrographs of the samples are shown Fig. 4 (a)-(d). The histogram analysis yields average particle size to be ~ 25 nm (BVO), ~ 23 nm (CBVO), ~ 18 nm (MBVO), and ~ 35 nm (CMBVO). The spherical shape of the particle remains relatively invariant in undoped, mono-doped, and co-doped NPs as expected due to high pH value during the synthesis [2,31,36,42,91]. The observed agglomerations across all the samples bear the signature of large surface energies of the NPs inevitable in hydrothermal synthesis

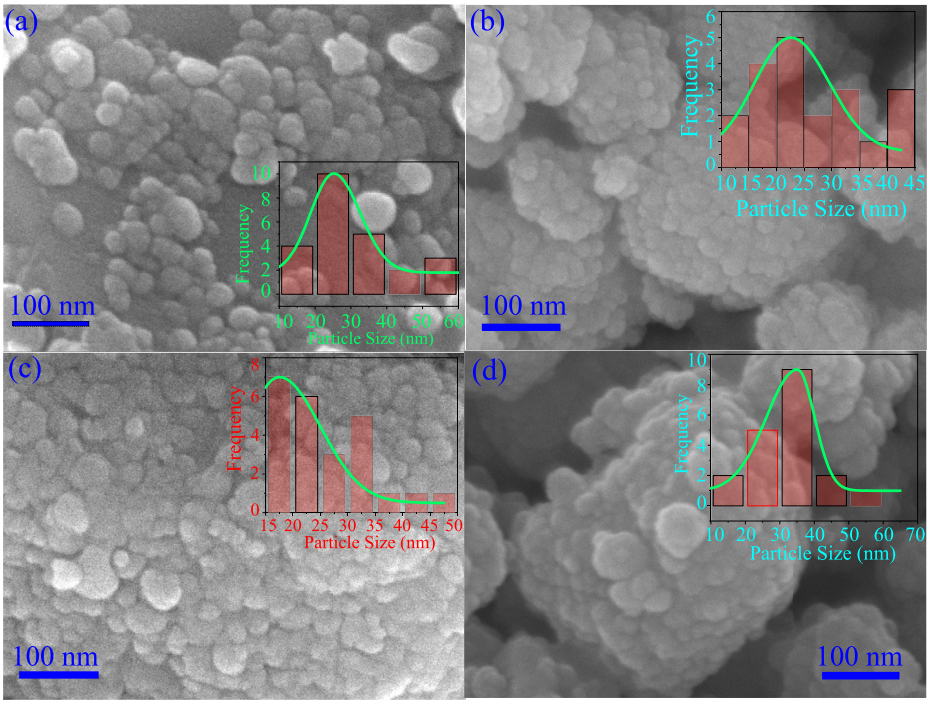

Fig. 4. FESEM micrographs of (a) BVO, (b) CBVO, (c) MBVO, and (d) CMBVO with particle size histograms superimposed.

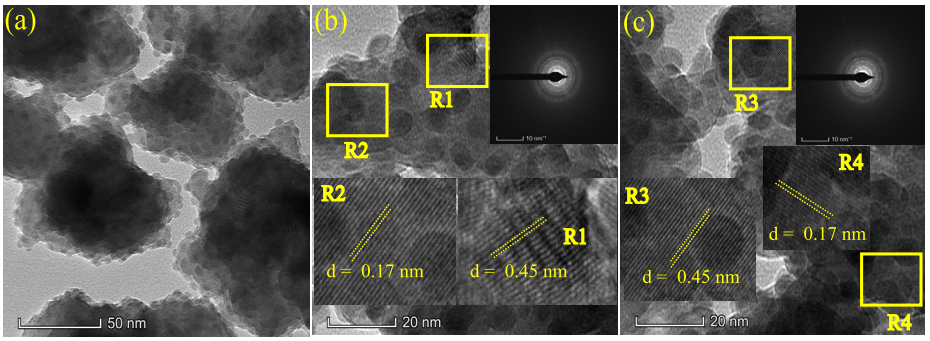

Fig. 5. (a) TEM and (b)-(c) HRTEM and SAED images CMBVO NPs.

[92]. The incorporation of Ce in CBVO and (Ce, Mo) in CMBVO inflates the irregular agglomerations and grain growths. This irregular agglomeration creates intra-agglomerate pores that may have reduced the specific surface area of the samples. This may hinder the photocatalytic performances of the CBVO and CMBVO, as we shall see in Section 3.8 [93]. In the Mo-doped MBVO NPs, the uniform compact agglomeration hinders the intra-agglomerate pore formation that may enhance the photocatalytic performance [94].

The morphology study was extended further for the CMBVO sample using TEM, High-Resolution TEM (HRTEM), and selective area electron diffraction (SAED) analysis as shown in Fig. 5(a)-(c). The spherical-shaped NPs were evident in the TEM image in Fig. 5(a). The polycrystalline nature of the CMBVO sample was confirmed by the SAED patterns in the insets of Fig. 5(b) and Fig. 5(c). The lattice fringes are visible in HRTEM images marked by yellow rectangular boxes R1 to R4. The lattice fringes with a spacing of 0.45 nm *d*-spacing in the regions R1 and R3 were characteristic of (1 1 −1) crystallographic plane of the *ms* phase. The *d*-spacing of 0.17 nm in the R2 region as displayed in Fig. 5(b) inset corresponds to (4 1 1)/ (0 6 1) crystallographic planes of *tz*/*ms* phases. The observed *d*-spacing of 0.29 nm in region R4 in Fig. 5(c) can be mapped to the (0 4 0)/ (2 1 1) crystallographic planes of *ms*/*tz* phases. Overall, the presence of mixed *ms*/*tz* phases along with the desired crystallographic planes in CMBVO was substantiated by the TEM analysis. The EDX spectra confirmed the elemental identifications of all samples as shown in Fig. S2-S3. Moreover, the uniform spatial distribution of the Ce and Mo dopants in CBVO, MBVO, and CMBVO samples was evident in Fig. S4-S6 which eliminates the possibility of spurious effects due to dopant segregation [95–100].

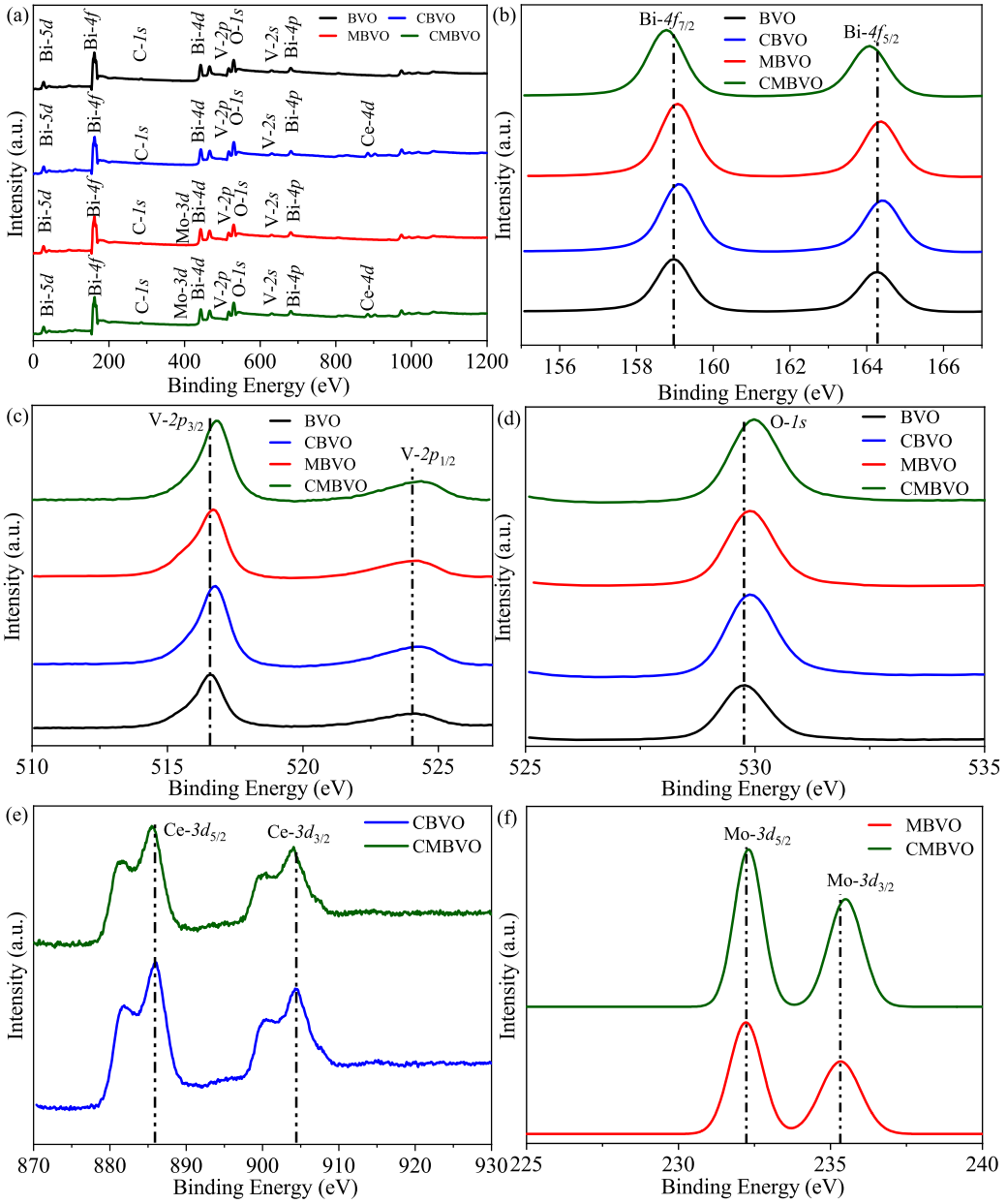

Fig. 6. (a) XPS Full Survey, Core level of (b) Bi-*4f*, (c) V-*2p* (d) O-*1s*, (e) Ce-*3d*, and (f) Mo-*3d* of BVO, CBVO, MBVO, and CMBVO NPs.

3.5. X-ray photoelectron spectroscopy

The full XPS spectra of BVO, CBVO, MBVO, and CMBVO displayed in Fig. 6(a) confirmed the presence of constituent Bi, V, O, Ce, and Mo elements. The Bi-*4f* XPS spectra of BVO in Fig. 6(b) revealed two distinct symmetrical peaks located at 159 and 164.3 eV owing to 5.3 eV spin-orbit split of the Bi-$4f_{7/2}$ and Bi-$4f_{5/2}$ [101,102]. The binding energies of these two XPS peaks are blue-shifted in both Ce and Mo mono-doped CBVO and MBVO, and red-shifted for co-doped CMBVO due to different electronegativities of the doping impurities [32]. The spin-split V-*3p* XPS lines at 516.6 and 524.1 eV of BVO in Fig. 6(c) were shifted to higher binding energies for mono-doped CBVO, MBVO, and co-doped CMBVO [103]. This shift was expected due to different electronegativities of Mo^{6+} and V^{5+} as well as changes in local coordination environments of Bi and V ions [8,97]. The core level O-*1s* of BVO exhibits a peak at a binding energy of 529.8 eV in Fig. 6(d) which can be attributed to the lattice oxygen [42]. The presence of Ce and Mo dopants blueshifted the bind energy of this XPS peak in cases of CBVO, MBVO, and CMBVO. The relative shift of Ce^{3+} XPS lines in Fig. 6(e) at binding energies (881.5, 885.7 eV) and (900.1, 904.2 eV) corresponding to Ce-$3d_{5/2}$ and Ce-$3d_{3/2}$ from CBVO to CMBVO was found to be nominal [31,104]. The binding energies of Mo-$3d_{5/2}$ and Mo-$3d_{3/2}$ at 232.2 and 235.4 eV respectively in Fig. 6(f) indicate the

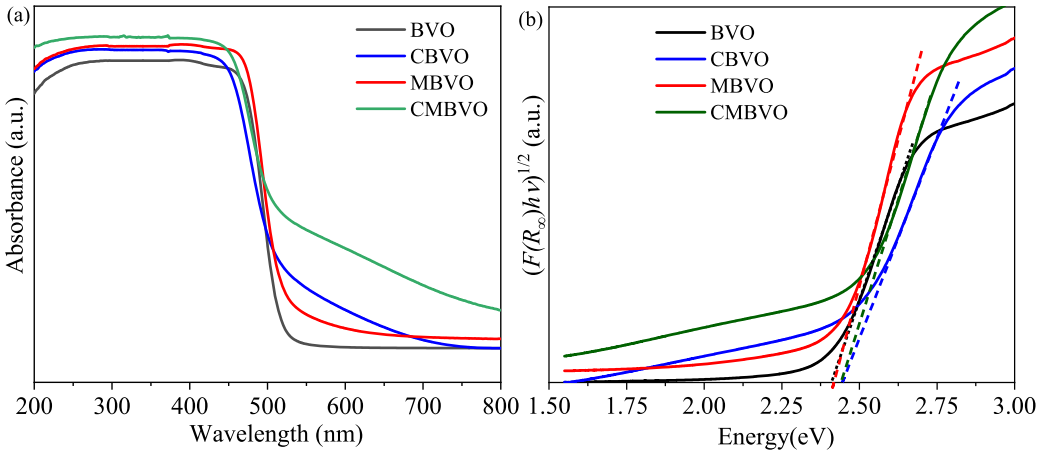

Fig. 7. (a) UV–Vis diffuse absorption spectra. (b) Band gap estimation from Tauc plot of BVO, CBVO, MBVO, and CMBVO NPs.

presence of Mo^{6+} oxidation state suitable for V-site in the sample as per the literature [32,97,105,106]. The binding energies of these XPS peaks have undergone a small red shift from MBVO to CMBVO. The Ce at% estimated from the XPS turned out to be 1.47 and 1.56 in CBVO and CMBVO, respectively which are quite close to the stoichiometric value of 1.67%. The at% of Mo was found to be 0.38 (CBVO) and 0.41 (CMBVO) at% which are in good agreement with the theoretical value of 0.33%.

3.6. UV-Vis spectroscopy

The measured UV-Vis diffuse reflectance was converted to absorption by using the Kubelka-Munk function $F(R_\infty)$ as displayed in Fig. 7(a) [107]. All samples have their primary absorption bands within the 450-550 nm wavelength range. The electronic band gap E_g and the photon energy $h\nu$ can be related with $F(R_\infty)$ as

$$[F(R_\infty)h\nu]^{1/\gamma} = A(h\nu - E_g), \tag{2}$$

where A is a constant, and the nature of the electronic transition is defined by the parameter γ [108–111]. The longer wavelength sub band gap optical absorption was significantly enhanced in the cases of CBVO and CMBVO NPs. The incorporation of Ce and (Ce, Mo) may have introduced defect states in the band gap that inflated the optical absorption leading to the Urbach tails in long wavelength region [112,113]. These deep sub-band defect states were substantiated by the DFT simulations in Section 3.9. Setting $\gamma = 2$ and extrapolating the steepest slopes of the Tauc plots to the energy axis as shown in Fig. 7(b), the indirect band gap was estimated to be 2.42, 2.45, 2.42, and 2.45 eV for BVO, CBVO, MBVO, and CMBVO samples, respectively. The estimated band gaps were consistent with that of the $BiVO_4$ [2,8,13,77,95,114,115]. The energy band gap remains essentially unchanged due to Ce doping in CBVO which is in line with the findings of Ref. [31,116,117].

3.7. Steady state photoluminescence measurements

Photoluminescence (PL) spectra encode information regarding photo-generated free electron-hole pair (EHP) recombination processes in materials [118]. The recombination of free charge carriers inside the material results in PL and thereby a strong correlation exists between PL emission intensity and the photocatalytic efficiencies [119,120]. Although the PL intensity can be affected by multiple factors like sample preparation conditions and impurity concentration, common observations suggest that low PL intensity implies a low free charge carrier recombination rate that promotes superior photocatalytic performances as more photo-generated carriers can participate in it [121–125]. The measured steady-state PL spectra of BVO, CBVO, MBVO, and CMBVO samples were displayed in Fig. 8. The PL emission of BVO near 525 nm marks the EHP recombination mediated by electron transition from the V-*3d* in the conduction band (CB) to the hole residing in the (Bi-*3d*, O-*2p*) hybridized states in the valence band (VB) of the *ms* phase [42,126]. The most intense PL peak occurred for CBVO sample which is indicative of enhanced EHP recombination in the presence of Ce dopants. The PL intensity diminishes gradually for CMBVO and MBVO, indicating a sequential reduction in photo-generated carrier recombination [127]. No significant PL peak shift in wavelength was observed for the mixed *ms-tz* phase of the CMBVO sample. This is expected as the PL peak of the *ms* phase lies very close to that of the *tz* phase [124,128]. The possible EHP recombination mechanism in these samples is explored from DFT simulations in Section 3.9.

3.8. Photocatalytic measurements

Fig. 9(a)-(d) present UV-vis MB dye absorption spectra as a function of irradiation time for BVO, CBVO, MBVO, and CMBVO photocatalysts. The MB characteristic 665 nm absorption peak intensity reduction over time corroborates the annihilation of its chromophoric structure by the photocatalyst. The dye degradation efficiencies of the photocatalysts were evaluated by recording

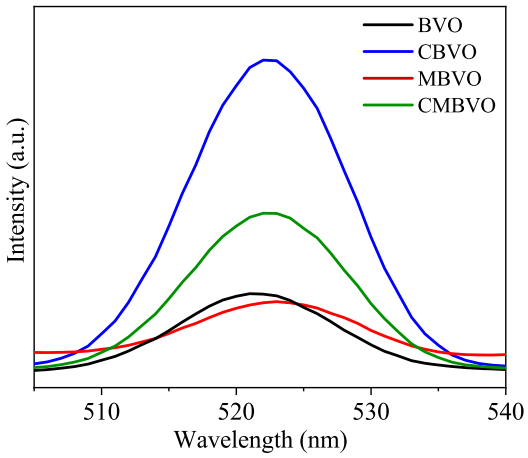

Fig. 8. Photoluminescence steady-state spectra of BVO, CBVO, MBVO, and CMBVO NPs measured at 260 nm excitation.

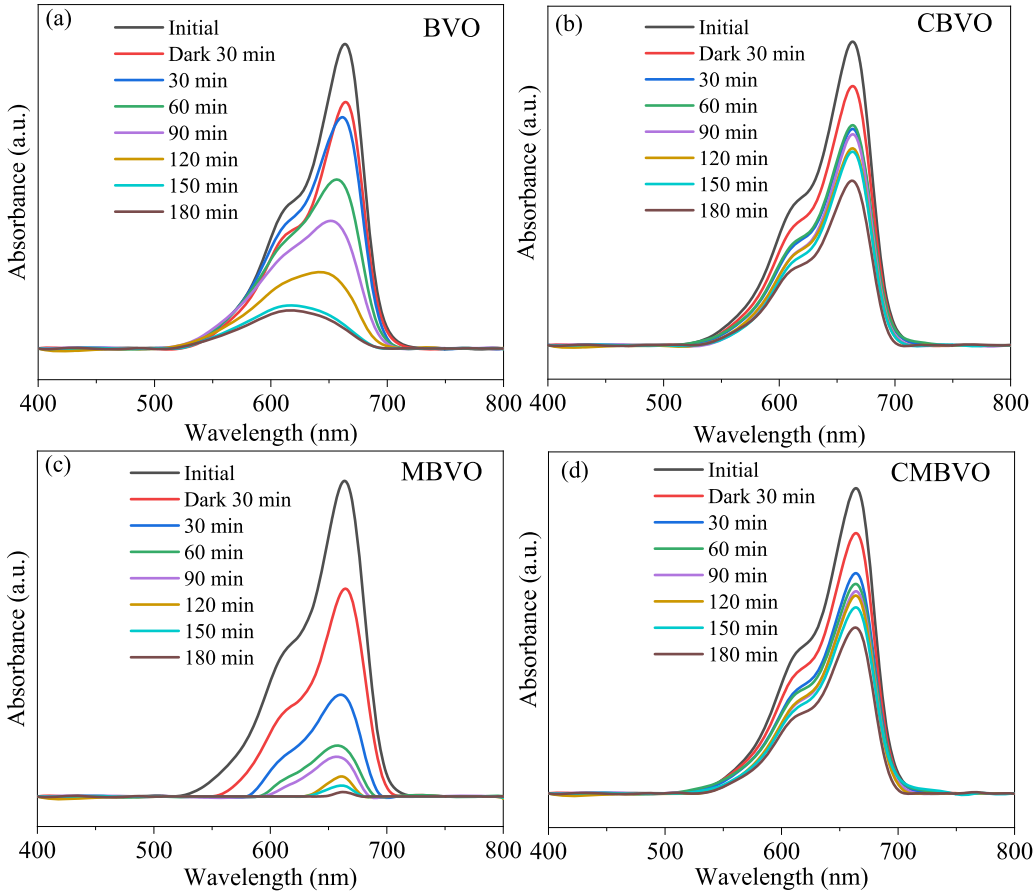

Fig. 9. The MB dye (10 ppm) degradation of 1 g/L (a) BVO, (b) CBVO, (c) MBVO, and (d) CMBVO photocatalysts measured from UV-vis absorption spectra during the photodegradation at pH = 10.

the ratio C/C_0, where C_0 and C stand for the MB concentration at initial and some specific time, as a function of simulated solar irradiation time as displayed in Fig. 10(a). For a comparative analysis of photocatalytic performances, the relevant parameters of interest were recorded from existing literature and this work in Table S7. The *ms* phase of the BVO achieved a 93% MB degradation efficiency, whereas *tz* phase has efficiencies < 40% in Ref. [28,42]. For CBVO, the 46% efficiency turned out to be low compared to that of Ref. [28]. The Mo mono-doped MBVO showed a 98% efficiency outperforming reported photocatalytic degradation efficiencies in Ref. [129–131]. For the co-doped CMBVO sample, the efficiency was reduced to 65%. The photocatalytic degradation can be

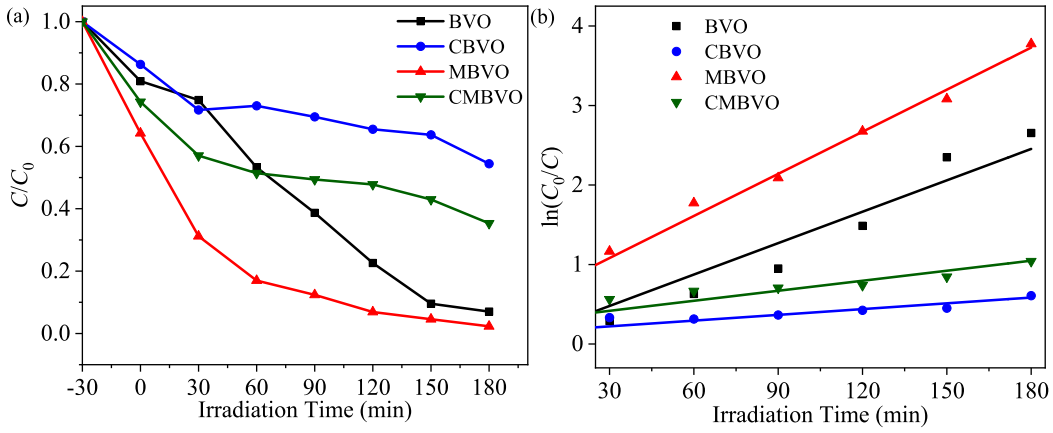

Fig. 10. (a) Time-dependent photocatalytic degradation fraction C/C_0 and (b) Linear fitted time-dependent photocatalytic degradation fraction of 10 ppm MB dye MB for 1 g/L BVO, CBVO, MBVO, and CMBVO photocatalyst as a function of irradiation time at pH = 10.

modeled with the pseudo-first-order kinetics following a time evolution of the C/C_0 as $\ln(C_0/C) = kt$ as depicted in Fig. 10(b). The slope of this linear fitting model provides the reaction rates k to be 0.01317 (BVO), 0.00242 (CBVO), 0.01765 (MBVO), and 0.00420 (CMBVO) min^{-1}. Several reasons can be speculated for the observed photocatalytic efficiency reduction in CBVO and CMBVO. The defect density measured from XRD analysis in Table S2 was increased in CMBVO which may adversely affect the photocatalytic performance. These defect states were supported by the Urbach tail in the UV-vis absorption data. In addition, the irregular agglomerations and grain growths in the CMBVO sample were presented in Section 3.4 can hinder the photocatalytic activity due to reduced specific surface area [93]. The DFT simulation presented in Section 3.9 suggests photo-generated carrier recombination may have adversely affected the photocatalytic performance of CBVO and CMBVO samples.

3.9. Electronic properties simulation

Fig. 11(a) presents the total density of states (TDOS) and its projections on relevant orbitals (PDOS) of pristine $BiVO_4$ supercell. The Fermi energy E_F was set as zero of energy. This DFT+U DOS yields band gap E_g of 2.51 eV. The energy states near the VBM stem from hybridization between dominant O-*2p* and small Bi-*6s* orbitals. The Bi-*5d* has negligible contribution to valence band maxima (VBM) and conduction band minima (CBm) edges. The states around the CBm originate from the mixing among large V-*3d*, small Bi-*6p*, and O-*2p* orbital contributions. The V-*3d* splits into two lobes in the CB due to the tetrahedron crystal-field effect. In the case of the 12.5% Ce doped $Bi_{0.875}Ce_{0.125}VO_4$ structure, the Ce-$4f$ orbital introduces deep impurity levels as shown in Fig. 11(b). The position of the impurity states in the electronic DOS depends on the choice of the Hubbard interaction parameter U and can produce energy levels deep in the energy band gap [31]. This impurity state can act as a photo-generated electron-hole pair recombination center and can effectively degrade the photocatalytic performance. The shallow up spin impurity states near the CB of Mo doped $BiV_{0.9375}Mo_{0.065}O_4$ in Fig. 11(c) germinated from the hybridization of Mo-*4d*, O-*2p* and V-*3d* orbitals. These states can trap photo-generated electrons preventing quick recombination and thereby prolonging its lifetime which may aid the photocatalytic activities. This Mo shallow trap states mediated carrier lifetime enhancement is well established in the existing literature [32,33,35,63]. For (12.5% Ce, 6.5% Mo) co-doped $Bi_{0.875}Ce_{0.125}V_{0.9375}Mo_{0.065}O_4$ structure, deep impurity states are created from the up spin of Ce-$4f^1$ states below the mid-band gap and the hybridization of Mo-*4d*, O-*2p* and V-*3d* stems impurity states above the mid-band gap region, see Fig. 11(d). These deep levels can inflate the unwanted carrier recombination that can act as a key factor in degrading the photocatalytic activity. The electronic BS is simulated along Γ, Z, D, B, A, and E high symmetry k-points for all aforementioned undoped and doped structures as shown in Fig. 12(a)-(d). The simulated indirect band gap E_g remained invariant at 2.62 eV. The deep impurity state due to Ce doping is evident in the BS of $Bi_{0.875}Ce_{0.125}VO_4$ as depicted in Fig. 12(b). The BS of Mo doped $BiV_{0.9375}Mo_{0.065}O_4$ structure in Fig. 12(c) shows the shallow impurity level near the CB as expected which can trap electrons and thereby prevent them from recombination. The (Ce, Mo) co-doped structure possesses detrimental deep recombination centers in its BS as presented in Fig. 12(d) that can limit the photocatalytic response.

Now we delve into the detailed analysis of the impurity stated in DOS that affects the photo-generated carriers. A trap center is amphoteric and can either trap an electron or a hole depending on its occupancy defined by its position relative to E_F [132–134]. In the case of the Ce-doped CBVO, the mid-gap Ce^{4+} defect states above the E_F is empty and act as electron recombination center as shown in Fig. 13(a). The photo-generated electron in the CB can recombine with the hole in the VB through the help of this recombination center through non-radiative Shockley-Read-Hall recombination [135]. For Mo-doped MBVO in Fig. 13(b), the empty Mo^{6+} state lies close to the CB and situated below the E_F. This level can trap the photo-generated electron and thereby hinder the EHP recombination. The trapped electron can easily be thermally excited to CB again and take part in photocatalytic reactions. In co-doped CMBVO, the Ce^{4+} and Mo^{6+} states, as shown in Fig. 13(c), are above the E_F. These empty states can mediate the non-radiative Shockley-Read-Hall electron-hole recombination and can prevent the EHP from taking part in photocatalytic activity.

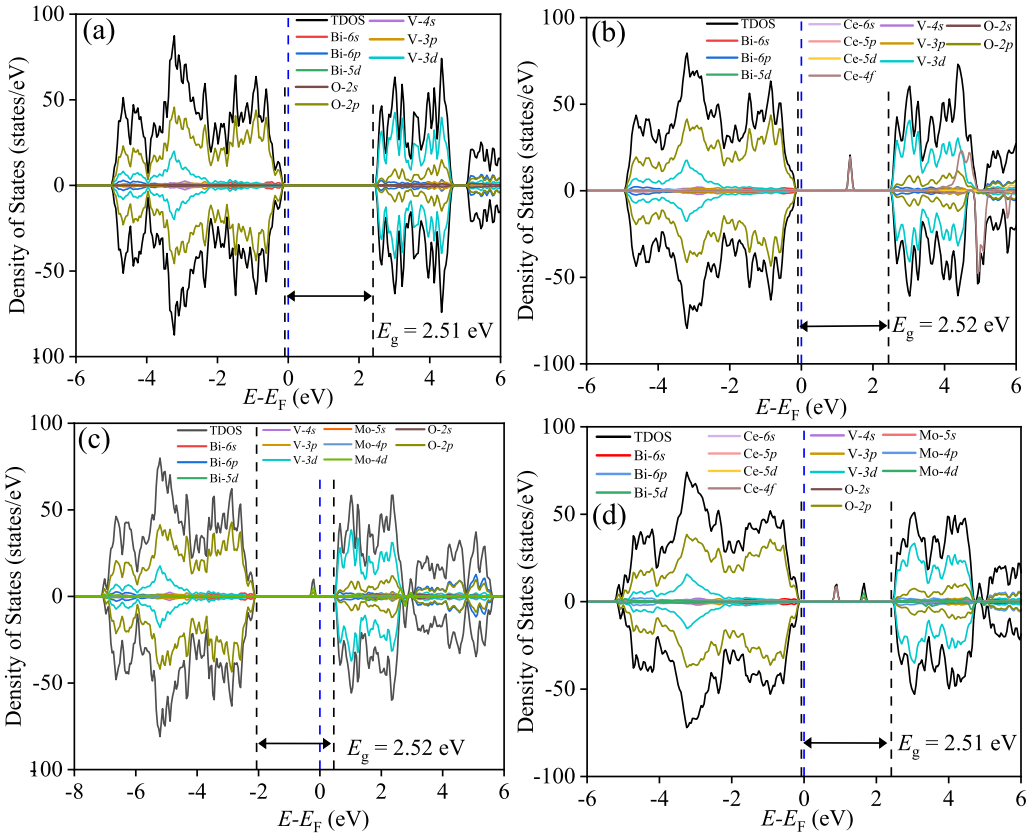

Fig. 11. The DFT+U derived TDOS and its projection onto different orbitals in Bi, V, O, Ce, and Mo atoms for (a) *ms* $BiVO_4$ supercell, (b) Ce doped $Bi_{0.875}Ce_{0.125}VO_4$ supercell, (c) Mo doped $BiV_{0.9375}Mo_{0.065}O_4$ supercell and (d) (Ce, Mo) co-doped $Bi_{0.875}Ce_{0.125}V_{0.9375}Mo_{0.065}O_4$ supercell.

4. Conclusion

The phases of hydrothermally synthesized undoped $BiVO_4$, 10% Ce doped $Bi_{0.90}Ce_{0.10}VO_4$, 2% Mo $BiV_{0.98}Mo_{0.02}O_4$ and (Ce = 10%, Mo = 2%) co-doped $Bi_{0.90}Ce_{0.10}V_{0.98}Mo_{0.02}O_4$ NPs were characterized with XRD, Raman, and FTIR spectroscopy. The FESEM micrographs revealed the NP sizes to be in the ~ 20 nm regime. The HRTEM and XPS have confirmed the (Ce, Mo) co-doping in mixed *ms-tz* phase of $Bi_{0.90}Ce_0.10V_{0.98}Mo_{0.02}O_4$. The spatial EDX scans confirmed uniform dopant distributions across the samples. The DRS confirmed the presence of defect states in (Ce, Mo) co-doped NPs as Urbach tails in the UV-vis absorption. The steady-state PL study provided evidence for enhancement in photo-generated carrier recombination in the (Ce, Mo) co-doped sample. This unwanted carrier recombination hampered its photocatalytic efficiency in MB dye degradation. The DFT+U simulation suggested the presence of Ce and Mo deep impurity states may act as recombination centers for the photo-generated carriers. Moreover, the increased defect densities, irregular agglomeration, and grain growth of the CMBVO sample may have hindered the photocatalytic activity. Overall, this work may have provided a detailed experimental analysis for (Ce, Mo) co-doped bismuth vanadate with theoretical perspectives.

CRediT authorship contribution statement

Tasnim Ahmed Mahi: Methodology, Investigation, Data curation. **Quazi Shafayat Hossain:** Software, Methodology, Investigation, Data curation. **Sadiq Shahriyar Nishat:** Software, Methodology, Investigation. **Shahran Ahmed:** Investigation. **M.N.I. Khan:** Resources, Methodology, Investigation. **Muhammad Shahriar Bashar:** Methodology, Investigation. **Shirin Akter Jahan:** Resources, Investigation, Formal analysis. **Umme Sarmeen Akhtar:** Investigation, Formal analysis. **Sharmin Jahan:** Methodology, Investigation. **Fariha Chowdhury:** Methodology, Investigation. **Khandker Saadat Hossain:** Methodology, Investigation. **Ahmad Irfan:** Methodology, Investigation. **Imtiaz Ahmed:** Writing – review & editing, Writing – original draft, Validation, Supervision, Software, Project administration, Funding acquisition, Formal analysis, Data curation, Conceptualization.

Declaration of competing interest

The authors declare that they have no known competing financial interests or personal relationships that could have appeared to influence the work reported in this paper.

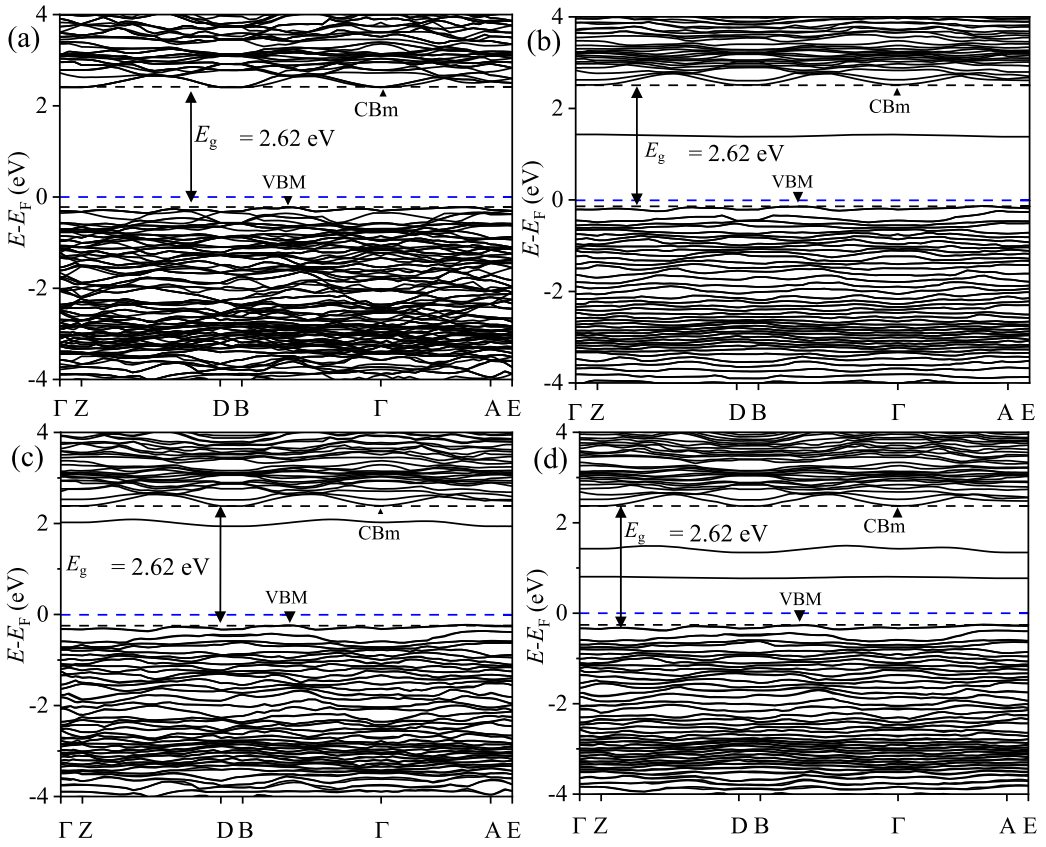

Fig. 12. Electronic BS of along Γ, Z, D, B, A, and E high symmetry k-points in BZ of (a) *ms* $BiVO_4$ supercell, (b) Ce doped $Bi_{0.875}Ce_{0.125}VO_4$ supercell, (c) Mo doped $BiV_{0.9375}Mo_{0.065}O_4$ supercell, and (d) (Ce, Mo) co-doped $Bi_{0.875}Ce_{0.125}V_{0.9375}Mo_{0.065}O_4$ supercell.

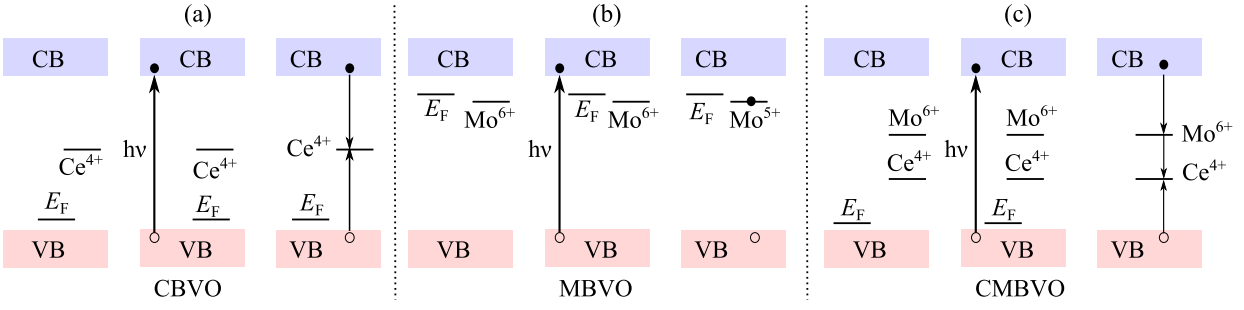

Fig. 13. Salient features of the electronic structure (a) CBVO, (b) MBVO, and (c) CMBVO in a schematic view. The reddish-filled and bluish-empty boxes represent the VB and CB, respectively. The black dot and the hollow circle denote electron and hole, respectively.

Data availability

The data that support the findings of this study are available from the corresponding author upon reasonable request.

Acknowledgements

I. Ahmed gratefully acknowledges financial support from the University Grants Commission (UGC) of Bangladesh Research Fund 2022-2023 for conducting the project. I. Ahmed thankfully extends his courtesy to the Bangladesh Research and Education Network (BdREN) for providing excellent and high-performance computational resources. I. Ahmed is very thankful to the Semiconductor Technology Research Centre, University of Dhaka for experimental support. I. Ahmed acknowledges resource-sharing support from Md. Shafiul Alam, Dept. of Electrical and Electronic Engineering, University of Dhaka. I. Ahmed would like to thank Md. Saiful Quddus, Institute of Glass and Ceramic Research and Testing (IGCRT), Bangladesh Council of Scientific and Industrial Research (BCSIR) regarding XPS measurements. I. Ahmed would like to thank M. A. Basith, Nanotechnology Research Laboratory, Department

of Physics, Bangladesh University of Engineering and Technology for facilitating the photoluminescence measurements. A. Irfan extends his appreciation to the Deanship of Scientific Research and graduate studies at King Khalid University Saudi Arabia for funding through the Large Research Groups Project under grant number (RGP2/156/45). K. S. Hossain acknowledges the support from the International Science Program (ISP), Uppsala University, Sweden. T.A. Mahi acknowledges a Research Fellowship from the Semiconductor Technology Research Centre, University of Dhaka.

Appendix A. Supplementary material

Supplementary material related to this article can be found online at https://doi.org/10.1016/j.heliyon.2024.e29408.

References

[1] Y. Park, K.J. McDonald, K.-S. Choi, Progress in bismuth vanadate photoanodes for use in solar water oxidation, Chem. Soc. Rev. 42 (6) (2013) 2321–2337.
[2] J.H. Kim, J.S. Lee, Elaborately modified $BiVO_4$ photoanodes for solar water splitting, Adv. Mater. 31 (20) (2019) 1806938.
[3] D. Chen, Z. Xie, Y. Tong, Y. Huang, Review on $BiVO_4$-based photoanodes for photoelectrochemical water oxidation: the main influencing factors, Energy Fuels 36 (17) (2022) 9932–9949.
[4] H.L. Tan, R. Amal, Y.H. Ng, Alternative strategies in improving the photocatalytic and photoelectrochemical activities of visible light-driven $BiVO_4$: a review, J. Mater. Chem. A 5 (32) (2017) 16498–16521.
[5] M. Tayebi, B.-K. Lee, Recent advances in $BiVO_4$ semiconductor materials for hydrogen production using photoelectrochemical water splitting, Renew. Sustain. Energy Rev. 111 (2019) 332–343.
[6] Z. Zhao, Z. Li, Z. Zou, Electronic structure and optical properties of monoclinic clinobisvanite $BiVO_4$, Phys. Chem. Chem. Phys. 13 (10) (2011) 4746–4753.
[7] A. Walsh, Y. Yan, M.N. Huda, M.M. Al-Jassim, S.-H. Wei, Band edge electronic structure of $BiVO_4$: elucidating the role of the Bi s and V d orbitals, Chem. Mater. 21 (3) (2009) 547–551.
[8] T.W. Kim, Y. Ping, G.A. Galli, K.-S. Choi, Simultaneous enhancements in photon absorption and charge transport of bismuth vanadate photoanodes for solar water splitting, Nat. Commun. 6 (1) (2015) 8769.
[9] S. Lardhi, L. Cavallo, M. Harb, Determination of the intrinsic defect at the origin of poor H_2 evolution performance of the monoclinic $BiVO_4$ photocatalyst using density functional theory, J. Phys. Chem. C 122 (32) (2018) 18204–18211.
[10] G.-L. Li, First-principles investigation of the surface properties of fergusonite-type monoclinic $BiVO_4$ photocatalyst, RSC Adv. 7 (15) (2017) 9130–9140.
[11] T. Liu, Q. Zhao, C. Li, Y. Lyu, M. Dupuis, Photocatalytic facet selectivity in $BiVO_4$ nanoparticles: polaron electronic structure and thermodynamic stability considerations for photocatalysis, J. Phys. Chem. C 123 (33) (2019) 20142–20151.
[12] T. Liu, M. Cui, M. Dupuis, Hole polaron transport in bismuth vanadate $BiVO_4$ from hybrid density functional theory, J. Phys. Chem. C 124 (42) (2020) 23038–23044.
[13] J. Fardush Tanha, S. Farhad, U. Honey, N. Tanvir, T. Hasan, S. Shahriyar Nishat, A. Kabir, S. Ahmed, M. Hakim, M. Khan, M. Moniruzzaman, I. Ahmed, A DFT+U look into experimentally synthesized monoclinic scheelite $BiVO_4$, J. Appl. Phys. 130 (23) (2021) 235107.
[14] J. Wiktor, I. Reshetnyak, F. Ambrosio, A. Pasquarello, Comprehensive modeling of the band gap and absorption spectrum of $BiVO_4$, Phys. Rev. Mater. 1 (2) (2017) 022401.
[15] I. Laraib, M.A. Carneiro, A. Janotti, Effects of doping on the crystal structure of $BiVO_4$, J. Phys. Chem. C 123 (44) (2019) 26752–26757.
[16] K.E. Kweon, G.S. Hwang, Hybrid density functional study of the structural, bonding, and electronic properties of bismuth vanadate, Phys. Rev. B 86 (16) (2012) 165209.
[17] K.E. Kweon, G.S. Hwang, Surface structure and hole localization in bismuth vanadate: a first principles study, Appl. Phys. Lett. 103 (13) (2013) 131603.
[18] J. Pellicer-Porres, D. Vazquez-Socorro, S. López-Moreno, A. Muñoz, P. Rodríguez-Hernández, D. Martínez-García, S.N. Achary, A.J. Rettie, C.B. Mullins, Phase transition systematics in $BiVO_4$ by means of high-pressure–high-temperature Raman experiments, Phys. Rev. B 98 (21) (2018) 214109.
[19] Y. Hu, D. Li, Y. Zheng, W. Chen, Y. He, Y. Shao, X. Fu, G. Xiao, $BiVO_4/TiO_2$ nanocrystalline heterostructure: a wide spectrum responsive photocatalyst towards the highly efficient decomposition of gaseous benzene, Appl. Catal. B 104 (1–2) (2011) 30–36.
[20] H. Xu, H. Li, C. Wu, J. Chu, Y. Yan, H. Shu, Z. Gu, Preparation, characterization and photocatalytic properties of Cu-loaded $BiVO_4$, J. Hazard. Mater. 153 (1–2) (2008) 877–884.
[21] M.-L. Guan, D.-K. Ma, S.-W. Hu, Y.-J. Chen, S.-M. Huang, From hollow olive-shaped $BiVO_4$ to n- p core-shell $BiVO_4@Bi_2O_3$ microspheres: controlled synthesis and enhanced visible-light-responsive photocatalytic properties, Inorg. Chem. 50 (3) (2011) 800–805.
[22] F.F. Abdi, S.P. Berglund, Recent developments in complex metal oxide photoelectrodes, J. Phys. D, Appl. Phys. 50 (19) (2017) 193002.
[23] F.F. Abdi, R. van de Krol, Nature and light dependence of bulk recombination in Co-Pi-catalyzed $BiVO_4$ photoanodes, J. Phys. Chem. C 116 (17) (2012) 9398–9404.
[24] F.F. Abdi, T.J. Savenije, M.M. May, B. Dam, R. van de Krol, The origin of slow carrier transport in $BiVO_4$ thin film photoanodes: a time-resolved microwave conductivity study, J. Phys. Chem. Lett. 4 (16) (2013) 2752–2757.
[25] W. Luo, Z. Li, T. Yu, Z. Zou, Effects of surface electrochemical pretreatment on the photoelectrochemical performance of Mo-doped $BiVO_4$, J. Phys. Chem. C 116 (8) (2012) 5076–5081.
[26] I. Grigioni, K.G. Stamplecoskie, E. Selli, P.V. Kamat, Dynamics of photogenerated charge carriers in $WO_3/BiVO_4$ heterojunction photoanodes, J. Phys. Chem. C 119 (36) (2015) 20792–20800.
[27] F. Lin, D. Wang, Z. Jiang, Y. Ma, J. Li, R. Li, C. Li, Photocatalytic oxidation of thiophene on $BiVO_4$ with dual co-catalysts Pt and RuO_2 under visible light irradiation using molecular oxygen as oxidant, Energy Environ. Sci. 5 (4) (2012) 6400–6406.
[28] S. Gu, W. Li, F. Wang, H. Li, H. Zhou, Substitution of Ce (III, IV) ions for Bi in $BiVO_4$ and its enhanced impact on visible light-driven photocatalytic activities, Catal. Sci. Technol. 6 (6) (2016) 1870–1881.
[29] S. Gu, W. Li, F. Wang, S. Wang, H. Zhou, H. Li, Synthesis of buckhorn-like $BiVO_4$ with a shell of CeO_x nanodots: effect of heterojunction structure on the enhancement of photocatalytic activity, Appl. Catal. B, Environ. 170 (2015) 186–194.
[30] D. Zhou, L.-X. Pang, J. Guo, Z.-M. Qi, T. Shao, Q.-P. Wang, H.-D. Xie, X. Yao, C.A. Randall, Influence of Ce substitution for Bi in $BiVO_4$ and the impact on the phase evolution and microwave dielectric properties, Inorg. Chem. 53 (2) (2014) 1048–1055.
[31] Z. Jiang, Y. Liu, T. Jing, B. Huang, X. Zhang, X. Qin, Y. Dai, M.-H. Whangbo, Enhancing the photocatalytic activity of $BiVO_4$ for oxygen evolution by Ce doping: Ce^{3+} ions as hole traps, J. Phys. Chem. C 120 (4) (2016) 2058–2063.
[32] K.P.S. Parmar, H.J. Kang, A. Bist, P. Dua, J.S. Jang, J.S. Lee, Photocatalytic and photoelectrochemical water oxidation over metal-doped monoclinic $BiVO_4$ photoanodes, ChemSusChem 5 (10) (2012) 1926–1934.
[33] J. Zhang, M. Deng, F. Ren, Y. Wu, Y. Wang, Effects of Mo/W codoping on the visible-light photocatalytic activity of monoclinic $BiVO_4$ within the GGA+U framework, RSC Adv. 6 (15) (2016) 12290–12297.

[34] W.-J. Yin, S.-H. Wei, M.M. Al-Jassim, J. Turner, Y. Yan, Doping properties of monoclinic $BiVO_4$ studied by first-principles density-functional theory, Phys. Rev. B 83 (15) (2011) 155102.

[35] K. Ding, B. Chen, Z. Fang, Y. Zhang, Z. Chen, Why the photocatalytic activity of Mo-doped $BiVO_4$ is enhanced: a comprehensive density functional study, Phys. Chem. Chem. Phys. 16 (26) (2014) 13465–13476.

[36] Y. Park, D. Kang, K.-S. Choi, Marked enhancement in electron–hole separation achieved in the low bias region using electrochemically prepared Mo-doped $BiVO_4$ photoanodes, Phys. Chem. Chem. Phys. 16 (3) (2014) 1238–1246.

[37] S.M. Thalluri, S. Hernandez, S. Bensaid, G. Saracco, N. Russo, Green-synthesized W-and Mo-doped $BiVO_4$ oriented along the {0 4 0} facet with enhanced activity for the sun-driven water oxidation, Appl. Catal. B, Environ. 180 (2016) 630–636.

[38] M. Rohloff, B. Anke, S. Zhang, U. Gernert, C. Scheu, M. Lerch, A. Fischer, Mo-doped $BiVO_4$ thin films–high photoelectrochemical water splitting performance achieved by a tailored structure and morphology, Sustain. Energy Fuels 1 (8) (2017) 1830–1846.

[39] M. Tayebi, A. Tayyebi, B.-K. Lee, Improved photoelectrochemical performance of molybdenum (Mo)-doped monoclinic bismuth vanadate with increasing donor concentration, Catal. Today 328 (2019) 35–42.

[40] C. Liu, H. Luo, Y. Xu, Z. Zhang, Q. Liang, W. Wang, Z. Chen, Synergistic cocatalytic effect of ultra-thin metal-organic framework and Mo-dopant for efficient photoelectrochemical water oxidation on $BiVO_4$ photoanode, Chem. Eng. J. 384 (2020) 123333.

[41] B.S. Kalanoor, H. Seo, S.S. Kalanur, Multiple ion doping in $BiVO_4$ as an effective strategy of enhancing photoelectrochemical water splitting: a review, Mater. Sci. Energy Technol. 4 (2021) 317–328.

[42] M. Noor, F. Sharmin, M. Al Mamun, S. Hasan, M. Hakim, M. Basith, Effect of Gd and Y co-doping in $BiVO_4$ photocatalyst for enhanced degradation of methylene blue dye, J. Alloys Compd. 895 (2022) 162639.

[43] C. Regmi, Y.K. Kshetri, S.K. Ray, R.P. Pandey, S.W. Lee, Utilization of visible to nir light energy by Yb^{+3}, Er^{+3} and Tm^{+3} doped $BiVO_4$ for the photocatalytic degradation of methylene blue, Appl. Surf. Sci. 392 (2017) 61–70.

[44] S. Obregón, G. Colón, Improved O_2 evolution from a water splitting reaction over Er^{+3} and Y^{+3} co-doped tetragonal $BiVO_4$, Catal. Sci. Technol. 4 (7) (2014) 2042–2050.

[45] J. Jia, M. Zhang, Z. Liu, C. Yu, W. Zhou, Z. Li, La^{3+}, Gd^{3+}-codoped $BiVO_4$ nanorods with superior visible-light-driven photocatalytic performance for simultaneous removing aqueous Cr (VI) and azo dye, J. Nanopart. Res. 22 (2020) 1–14.

[46] Y. Liu, L. Meng, H. Wang, J. Jiao, M. Xing, Y. Peng, X. Luo, Y. Tian, Promising lanthanide-doped $BiVO_4$ phosphors for highly efficient upconversion luminescence and temperature sensing, Dalton Trans. 50 (3) (2021) 960–969.

[47] J.-S. Ma, L.-Y. Lin, Y.-S. Chen, Facile solid-state synthesis for producing molybdenum and tungsten co-doped monoclinic $BiVO_4$ as the photocatalyst for photoelectrochemical water oxidation, Int. J. Hydrog. 44 (16) (2019) 7905–7914.

[48] X. Zhao, J. Hu, B. Wu, A. Banerjee, S. Chakraborty, J. Feng, Z. Zhao, S. Chen, R. Ahuja, T.C. Sum, Z. Chen, Simultaneous enhancement in charge separation and onset potential for water oxidation in a $BiVO_4$ photoanode by W–Ti codoping, J. Mater. Chem. A 6 (35) (2018) 16965–16974.

[49] Z. Jiao, J. Zheng, C. Feng, Z. Wang, X. Wang, G. Lu, Y. Bi, Fe/W co-doped $BiVO_4$ photoanodes with a metal–organic framework cocatalyst for improved photoelectrochemical stability and activity, ChemSusChem 9 (19) (2016) 2824–2831.

[50] S. Saxena, A. Verma, N.K. Biswas, S.A. Khan, V.R. Satsangi, R. Shrivastav, S. Dass, Zr–W co-doping in $BiVO_4$–synergistic effect in photoelectrochemical water splitting, Mater. Chem. Phys. 267 (2021) 124675.

[51] G. Kaur, K. Asha, S. Dass, R. Shrivastav, Photoelectrochemical performance of Yb co-doped $BiV_{0.98}Mo_{0.02}O_4$ thin films for photoelectrochemical water splitting, Mater. Today Proc. 49 (2022) 738–743.

[52] W. Luo, Z. Yang, Z. Li, J. Zhang, J. Liu, Z. Zhao, Z. Wang, S. Yan, T. Yu, Z. Zou, Solar hydrogen generation from seawater with a modified $BiVO_4$ photoanode, Energy Environ. Sci. 4 (10) (2011) 4046–4051.

[53] W. Zhang, F. Wu, J. Li, D. Yan, J. Tao, Y. Ping, M. Liu, Unconventional relation between charge transport and photocurrent via boosting small polaron hopping for photoelectrochemical water splitting, ACS Energy Lett. 3 (9) (2018) 2232–2239.

[54] G. Kresse, J. Furthmüller, Efficient iterative schemes for ab initio total-energy calculations using a plane-wave basis set, Phys. Rev. B 54 (16) (1996) 11169.

[55] G. Kresse, D. Joubert, From ultrasoft pseudopotentials to the projector augmented-wave method, Phys. Rev. B 59 (3) (1999) 1758.

[56] A. Jain, Y. Shin, K.A. Persson, Computational predictions of energy materials using density functional theory, Nat. Rev. Mater. 1 (1) (2016) 1–13.

[57] R.O. Jones, Density functional theory: its origins, rise to prominence, and future, Rev. Mod. Phys. 87 (3) (2015) 897.

[58] M.Z. Hossain, S.S. Nishat, S. Ahmed, Q.S. Hossain, M. Khan, T. Hasan, M.S. Bashar, A.S.H. Faysal, I.M. Syed, K.S. Hossain, S. Hussain, M.M. Khan, I. Ahmed, Combined experimental and DFT approach to $BiNbO_4$ polymorphs, RSC Adv. 13 (8) (2023) 5576–5589.

[59] Q.S. Hossain, S. Ahmed, S.S. Nishat, M.Z. Hossain, M. Khan, T. Hasan, M.S. Bashar, M. Hakim, I.M. Syed, K.S. Hossain, I. Ahmed, An ab initio DFT perspective on experimentally synthesized $CuBi_2O_4$, RSC Adv. 13 (21) (2023) 14291–14305.

[60] S. Ahmed, S.S. Nishat, A. Kabir, A.S.H. Faysal, T. Hasan, S. Chakraborty, I. Ahmed, Structural, elastic, vibrational, electronic and optical properties of $SmFeO_3$ using density functional theory, Physica B, Condens. Matter 615 (2021) 413061.

[61] S. Ahmed, T. Hasan, A.S.H. Faysal, S.S. Nishat, M. Khan, A. Kabir, I. Ahmed, A DFT+U approach to doped $SrTiO_3$ for solar harvesting applications, Comput. Mater. Sci. 214 (2022) 111743.

[62] Q.S. Hossain, S.S. Nishat, M. Sultana, T.A. Mahi, S. Ahmed, M. Khan, H. Das, M.S. Bashar, U.S. Akhtar, S. Jahan, F. Chowdhury, K.S. Hossain, S.M.S. Imran, I. Ahmed, A combined first principles and experimental approach to Bi_2WO_6, RSC Adv. 13 (51) (2023) 36130–36143.

[63] H.S. Park, K.E. Kweon, H. Ye, E. Paek, G.S. Hwang, A.J. Bard, Factors in the metal doping of $BiVO_4$ for improved photoelectrocatalytic activity as studied by scanning electrochemical microscopy and first-principles density-functional calculation, J. Phys. Chem. C 115 (36) (2011) 17870–17879.

[64] I. Solovyev, P. Dederichs, V. Anisimov, Corrected atomic limit in the local-density approximation and the electronic structure of d impurities in Rb, Phys. Rev. B 50 (23) (1994) 16861.

[65] M. Farouk, A. Samir, F. Metawe, M. Elokr, Optical absorption and structural studies of bismuth borate glasses containing Er^{3+} ions, J. Non-Cryst. Solids 371 (2013) 14–21.

[66] Y. Qi, M. Wang, Y. Zhang, T. Zhu, Effect of calcination temperature on the structure and photocatalytic performance of $BiVO_4$ prepared via an improved solution combustion method, Nano-Micro Lett. 13 (7) (2018) 1017–1020.

[67] H.-q. Jiang, H. Endo, H. Natori, M. Nagai, K. Kobayashi, Fabrication and photoactivities of spherical-shaped $BiVO_4$ photocatalysts through solution combustion synthesis method, J. Eur. Ceram. Soc. 28 (15) (2008) 2955–2962.

[68] H.A. Abbood, A. Alabdie, A. Al-Hawash, A.A. Abbood, K. Huang, Fabrication of double-sided comb-like F/Ce co-doped $BiVO_4$ micro/nanostructures for enhanced photocatalytic degradation and water oxidation, J. Nanopart. Res. 22 (2020) 1–13.

[69] I. Abdellaoui, M.M. Islam, M. Remeika, Y. Higuchi, T. Kawaguchi, T. Harada, C. Budich, T. Maeda, T. Wada, S. Ikeda, et al., Photocarrier recombination dynamics in $BiVO_4$ for visible light-driven water oxidation, J. Phys. Chem. C 124 (7) (2020) 3962–3972.

[70] A. Bhattacharya, K. Mallick, A. Hartridge, Phase transition in $BiVO_4$, Mater. Lett. 30 (1) (1997) 7–13.

[71] X. Li, L. Xu, X. Li, M. Hu, R. Huang, C. Huang, Oxidant peroxo-synthesized monoclinic $BiVO_4$: insights into the crystal structure deformation and the thermochromic properties, J. Alloys Compd. 787 (2019) 666–671.

[72] Y. Lin, C. Lu, C. Wei, Microstructure and photocatalytic performance of $BiVO_4$ prepared by hydrothermal method, J. Alloys Compd. 781 (2019) 56–63.

[73] G. Tan, L. Zhang, H. Ren, S. Wei, J. Huang, A. Xia, Effects of ph on the hierarchical structures and photocatalytic performance of $BiVO_4$ powders prepared via the microwave hydrothermal method, ACS Appl. Mater. Interfaces 5 (11) (2013) 5186–5193.

[74] L. Zhou, W. Wang, L. Zhang, H. Xu, W. Zhu, Single-crystalline bivo4 microtubes with square cross-sections: microstructure, growth mechanism, and photocatalytic property, J. Phys. Chem. C 111 (37) (2007) 13659–13664.

[75] L. Avakyants, A. Chervyakov, V. Gorelik, P. Sverbil, Inelastic light scattering near the ferroelectric phase-transition point in bismuth vanadate crystals, J. Russ. Laser Res. 25 (6) (2004) 535–580.

[76] P. Subramanyam, T. Vinodkumar, D. Nepak, M. Deepa, C. Subrahmanyam, Mo-doped $BiVO_4$ reduced graphene oxide composite as an efficient photoanode for photoelectrochemical water splitting, Catal. Today 325 (2019) 73–80.

[77] E. Alarcón-Lladó, L. Chen, M. Hettick, N. Mashouf, Y. Lin, A. Javey, J.W. Ager, $BiVO_4$ thin film photoanodes grown by chemical vapor deposition, Phys. Chem. Chem. Phys. 16 (4) (2014) 1651–1657.

[78] J. Yu, A. Kudo, Effects of structural variation on the photocatalytic performance of hydrothermally synthesized $BiVO_4$, Adv. Funct. Mater. 16 (16) (2006) 2163–2169.

[79] T.S. Dabodiya, P. Selvarasu, A.V. Murugan, Tetragonal to monoclinic crystalline phases change of $BiVO_4$ via microwave-hydrothermal reaction: in correlation with visible-light-driven photocatalytic performance, Inorg. Chem. 58 (8) (2019) 5096–5110.

[80] R.L. Frost, D.A. Henry, M.L. Weier, W. Martens, Raman spectroscopy of three polymorphs of $BiVO_4$: clinobisvanite, dreyerite and pucherite, with comparisons to -bearing minerals: namibite, pottsite and schumacherite, J. Raman Spectrosc. 37 (7) (2006) 722–732.

[81] S. Usai, S. Obregón, A.I. Becerro, G. Colón, Monoclinic–tetragonal heterostructured $BiVO_4$ by yttrium doping with improved photocatalytic activity, J. Phys. Chem. C 117 (46) (2013) 24479–24484.

[82] P. Pookmanee, S. Kojinok, R. Puntharod, S. Sangsrichan, S. Phanichphant, Preparation and characterization of $BiVO_4$ powder by the sol-gel method, Ferroelectrics 456 (1) (2013) 45–54.

[83] M. Gotić, S. Musić, M. Ivanda, M. Šoufek, S. Popović, Synthesis and characterisation of bismuth (III) vanadate, J. Mol. Struct. 744 (2005) 535–540.

[84] K. Hirota, G. Komatsu, M. Yamashita, H. Takemura, O. Yamaguchi, Formation, characterization and sintering of alkoxy-derived bismuth vanadate, Mater. Res. Bull. 27 (7) (1992) 823–830.

[85] D. Ke, T. Peng, L. Ma, P. Cai, K. Dai, Effects of hydrothermal temperature on the microstructures of $BiVO_4$ and its photocatalytic O_2 evolution activity under visible light, Inorg. Chem. 48 (11) (2009) 4685–4691.

[86] A. Zhang, J. Zhang, The effect of hydrothermal temperature on the synthesis of monoclinic bismuth vanadate powders, Mater. Sci. Pol. 27 (4/1) (2009).

[87] S. Beg, N.A. Al-Areqi, Structural and electrical study of Ce^{IV}-substituted bismuth vanadate, J. Phys. Chem. Solids 70 (6) (2009) 1000–1007.

[88] A.K. Warrier, B. Kulkarni, K. Amrutha, D. Jayaram, G. Valsan, P. Agarwal, Seasonal variations in the abundance and distribution of microplastic particles in the surface waters of a southern Indian lake, Chemosphere 300 (2022) 134556.

[89] S. Li, Y. Cheng, Q. Wang, C. Liu, L. Xu, Design, fabrication and characterization of photocatalyst Ni-doped $BiVO_4$ for high effectively degrading dye contaminant, Mater. Res. Express 7 (11) (2020) 115005.

[90] D.P. Jaihindh, B. Thirumalraj, S.-M. Chen, P. Balasubramanian, Y.-P. Fu, Facile synthesis of hierarchically nanostructured bismuth vanadate: an efficient photocatalyst for degradation and detection of hexavalent chromium, J. Hazard. Mater. 367 (2019) 647–657.

[91] Y. Guo, X. Yang, F. Ma, K. Li, L. Xu, X. Yuan, Y. Guo, Additive-free controllable fabrication of bismuth vanadates and their photocatalytic activity toward dye degradation, Appl. Surf. Sci. 256 (7) (2010) 2215–2222.

[92] Y. Luo, G. Tan, G. Dong, H. Ren, A. Xia, Effects of structure, morphology, and up-conversion on Nd-doped $BiVO_4$ system with high photocatalytic activity, Ceram. Int. 41 (2) (2015) 3259–3268.

[93] X. Wang, Y. Shen, G. Zuo, F. Li, Y. Meng, Influence of heat treatment on photocatalytic performance of $BiVO_4$ synthesised by sol–gel method, Mater. Technol. 31 (3) (2016) 176–180.

[94] M. Du Plessis, Relationship between specific surface area and pore dimension of high porosity nanoporous silicon–model and experiment, Phys. Status Solidi 204 (7) (2007) 2319–2328.

[95] V.-I. Merupo, S. Velumani, K. Ordon, N. Errien, J. Szade, A.-H. Kassiba, Structural and optical characterization of ball-milled copper-doped bismuth vanadium oxide ($BiVO_4$), CrystEngComm 17 (17) (2015) 3366–3375.

[96] M. Beetz, S. Häringer, P. Elsässer, J. Kampmann, L. Sauerland, F. Wolf, M. Günther, A. Fischer, T. Bein, Ultra-thin protective coatings for sustained photoelectrochemical water oxidation with Mo: $BiVO_4$, Adv. Funct. Mater. 31 (45) (2021) 2011210.

[97] S.S. Mali, G.R. Park, H. Kim, H.H. Kim, J.V. Patil, C.K. Hong, Synthesis of nanoporous Mo:$BiVO_4$ thin film photoanodes using the ultrasonic spray technique for visible-light water splitting, Nanoscale Adv. 1 (2) (2019) 799–806.

[98] J. Jian, Y. Xu, X. Yang, W. Liu, M. Fu, H. Yu, F. Xu, F. Feng, L. Jia, D. Friedrich, et al., Embedding laser generated nanocrystals in $BiVO_4$ photoanode for efficient photoelectrochemical water splitting, Nat. Commun. 10 (1) (2019) 2609.

[99] S. Ahmed, A.S.H. Faysal, M. Khan, M. Basith, M.S. Bashar, H. Das, T. Hasan, I. Ahmed, Room temperature ferroic orders in Zr and (Zr, Ni) doped $SrTiO_3$, Results Phys. 31 (2021) 104940.

[100] M. Valant, T. Kolodiazhnyi, I. Arčon, F. Aguesse, A.-K. Axelsson, N.M. Alford, The origin of magnetism in Mn-doped $SrTiO_3$, Adv. Funct. Mater. 22 (10) (2012) 2114–2122.

[101] A.P. Singh, N. Kodan, A. Dey, S. Krishnamurthy, B.R. Mehta, Improvement in the structural, optical, electronic and photoelectrochemical properties of hydrogen treated bismuth vanadate thin films, Int. J. Hydrog. 40 (12) (2015) 4311–4319.

[102] H.L. Tan, A. Suyanto, A.T.D. Denko, W.H. Saputera, R. Amal, F.E. Osterloh, Y.H. Ng, Enhancing the photoactivity of faceted $BiVO_4$ via annealing in oxygen-deficient condition, Part. Part. Syst. Charact. 34 (4) (2017) 1600290.

[103] Y. Luo, G. Tan, G. Dong, H. Ren, A. Xia, A comprehensive investigation of tetragonal Gd-doped $BiVO_4$ with enhanced photocatalytic performance under sun-light, Appl. Surf. Sci. 364 (2016) 156–165.

[104] J. Wu, L. Yin, L. Zhang, Tuning the electronic structure, band gap energy and photoluminescence properties of hexagonal boron nitride nanosheets via a controllable Ce^{3+} ions doping, RSC Adv. 3 (20) (2013) 7408–7418.

[105] W. Luo, J. Wang, X. Zhao, Z. Zhao, Z. Li, Z. Zou, Formation energy and photoelectrochemical properties of $BiVO_4$ after doping at Bi^{3+} or V^{5+} sites with higher valence metal ions, Phys. Chem. Chem. Phys. 15 (3) (2013) 1006–1013.

[106] L. Wang, X. Gu, Y. Zhao, M. Wei, Y. Qiang, Y. Zhao, Enhanced photoelectrochemical performance by doping Mo into $BiVO_4$ lattice, J. Mater. Sci., Mater. Electron. 29 (2018) 19278–19286.

[107] P. Kubelka, F. Munk, A contribution to the optics of pigments, Z. Technol. Phys. 12 (593) (1931) 193.

[108] J. Tauc, R. Grigorovici, A. Vancu, Optical properties and electronic structure of amorphous germanium, Phys. Status Solidi B 15 (2) (1966) 627–637.

[109] J.I. Pankove, D.A. Kiewit, Optical processes in semiconductors, J. Electrochem. Soc. 119 (5) (1972) 156Ca.

[110] R. López, R. Gómez, Band-gap energy estimation from diffuse reflectance measurements on sol–gel and commercial TiO_2: a comparative study, J. Sol-Gel Sci. Technol. 61 (1) (2012) 1–7.

[111] P. Makuła, M. Pacia, W. Macyk, How to correctly determine the band gap energy of modified semiconductor photocatalysts based on UV–Vis spectra, J. Phys. Chem. Lett. 09 (2018) 6814–6817.

[112] A. Podborska, B. Gaweł, Ł. Pietrzak, I.B. Szymanska, J.K. Jeszka, W. Łasocha, K. Szaciłowski, Anomalous photocathodic behavior of CdS within the urbach tail region, J. Phys. Chem. C 113 (16) (2009) 6774–6784.

[113] P. Kwolek, K. Pilarczyk, T. Tokarski, K. Lewandowska, K. Szaciłowski, $Bi_xLa_{(1-x)}VO_4$ solid solutions: tuning of electronic properties via stoichiometry modifications, Nanoscale 6 (4) (2014) 2244–2254.

[114] S. Wang, T. He, P. Chen, A. Du, K. Ostrikov, W. Huang, L. Wang, In situ formation of oxygen vacancies achieving near-complete charge separation in planar $BiVO_4$ photoanodes, Adv. Mater. 32 (26) (2020) 2001385.
[115] L.S. Kumari, P.P. Rao, A.N.P. Radhakrishnan, V. James, S. Sameera, P. Koshy, Brilliant yellow color and enhanced nir reflectance of monoclinic $BiVO_4$ through distortion in VO_4^{3-} tetrahedra, Sol. Energy Mater. Sol. Cells 112 (2013) 134–143.
[116] H. Xu, C. Wu, H. Li, J. Chu, G. Sun, Y. Xu, Y. Yan, Synthesis, characterization and photocatalytic activities of rare Earth-loaded $BiVO_4$ catalysts, Appl. Surf. Sci. 256 (3) (2009) 597–602.
[117] X.-L. Luo, C.-J. Liu, M.-J. Chen, S.-S. Zhang, Y.-H. Xu, Electrochemical performance and enhanced photocatalytic activity of Ce-doped $BiVO_4$ under visible light irradiation, Mater. Res. Bull. 94 (2017) 428–434.
[118] J.-Q. Li, Z.-Y. Guo, H. Liu, J. Du, Z.-F. Zhu, Two-step hydrothermal process for synthesis of F-doped $BiVO_4$ spheres with enhanced photocatalytic activity, J. Alloys Compd. 581 (2013) 40–45.
[119] J.C. Yu, J. Yu, W. Ho, Jiang, Zhang, Effects of F-doping on the photocatalytic activity and microstructures of nanocrystalline TiO_2 powders, Chem. Mater. 14 (9) (2002) 3808–3816.
[120] R. Georgekutty, M.K. Seery, S.C. Pillai, A highly efficient Ag-ZnO photocatalyst: synthesis, properties, and mechanism, J. Phys. Chem. C 112 (35) (2008) 13563–13570.
[121] Q.C. Xu, D.V. Wellia, Y.H. Ng, R. Amal, T.T.Y. Tan, Synthesis of porous and visible-light absorbing Bi_2WO_6/TiO_2 heterojunction films with improved photo-electrochemical and photocatalytic performances, J. Phys. Chem. C 115 (15) (2011) 7419–7428.
[122] L. Chen, S.-F. Yin, R. Huang, Q. Zhang, S.-L. Luo, C.-T. Au, Hollow peanut-like m-$BiVO_4$: facile synthesis and solar-light-induced photocatalytic property, CrystEngComm 14 (12) (2012) 4217–4222.
[123] H. Cheng, B. Huang, Y. Dai, X. Qin, X. Zhang, One-step synthesis of the nanostructured AgI/BiOI composites with highly enhanced visible-light photocatalytic performances, Langmuir 26 (9) (2010) 6618–6624.
[124] C. Yu, K. Yang, C.Y. Jimmy, F. Cao, X. Li, X. Zhou, Fast fabrication of Co_3O_4 and $CuO/BiVO_4$ composite photocatalysts with high crystallinity and enhanced photocatalytic activity via ultrasound irradiation, J. Alloys Compd. 509 (13) (2011) 4547–4552.
[125] L. Chen, Q. Zhang, R. Huang, S.-F. Yin, S.-L. Luo, C.-T. Au, Porous peanut-like Bi_2O_3–$BiVO_4$ composites with heterojunctions: one-step synthesis and their photocatalytic properties, Dalton Trans. 41 (31) (2012) 9513–9518.
[126] C. Yu, S. Dong, J. Zhao, X. Han, J. Wang, J. Sun, Preparation and characterization of sphere-shaped $BiVO_4$/reduced graphene oxide photocatalyst for an augmented natural sunlight photocatalytic activity, J. Alloys Compd. 677 (2016) 219–227.
[127] Z. Zhang, M. Wang, W. Cui, H. Sui, Synthesis and characterization of a core–shell $BiVO_4$@g-C_3N_4 photo-catalyst with enhanced photocatalytic activity under visible light irradiation, RSC Adv. 7 (14) (2017) 8167–8177.
[128] A. Kudo, K. Omori, H. Kato, A novel aqueous process for preparation of crystal form-controlled and highly crystalline $BiVO_4$ powder from layered vanadates at room temperature and its photocatalytic and photophysical properties, J. Am. Chem. Soc. 121 (49) (1999) 11459–11467.
[129] B. Liu, X. Yan, H. Yan, Y. Yao, Y. Cai, J. Wei, S. Chen, X. Xu, L. Li, Preparation and characterization of Mo doped in $BiVO_4$ with enhanced photocatalytic properties, Materials 10 (8) (2017) 976.
[130] V.G. Warrier, J. Devasia, A. Nizam, V. VL, G. Nagendra, Facile combustion synthesis of highly active Mo doped $BiVO_4$ for photocatalytic dye degradation, photo-oxidation of alcohols, antifungal and antioxidant activities, Int. J. Environ. Anal. Chem. (2022) 1–20.
[131] C.-Y. Tsay, C.-Y. Chung, C.-Y. Chen, Y.-C. Chang, C.-J. Chang, J.J. Wu, Enhanced photocatalytic performance of visible-light-driven $BiVO_4$ nanoparticles through W and Mo substituting, Catalysts 13 (3) (2023) 475.
[132] J. Simmons, G. Taylor, Nonequilibrium steady-state statistics and associated effects for insulators and semiconductors containing an arbitrary distribution of traps, Phys. Rev. B 4 (2) (1971) 502.
[133] B. Streetman, Carrier recombination and trapping effects in transient photoconductive decay measurements, J. Appl. Phys. 37 (8) (1966) 3137–3144.
[134] J. Jiang, C. Ling, T. Xu, W. Wang, X. Niu, A. Zafar, Z. Yan, X. Wang, Y. You, L. Sun, et al., Defect engineering for modulating the trap states in 2D photoconductors, Adv. Mater. 30 (40) (2018) 1804332.
[135] W. Shockley, W. Read Jr, Statistics of the recombinations of holes and electrons, Phys. Rev. 87 (5) (1952) 835.